

# GOING BEYOND $S_8$ : FAST INFERENCE OF THE MATTER POWER SPECTRUM FROM WEAK-LENSING SURVEYS

CYRILLE DOUX<sup>✉</sup>

Université Grenoble Alpes, CNRS, LPSC-IN2P3, 38000 Grenoble, France

TANVI KARWAL<sup>✉</sup>

Kavli Institute for Cosmological Physics, Enrico Fermi Institute, and Department of Astronomy & Astrophysics, University of Chicago, Chicago IL 60637  
Version January 7, 2026

## Abstract

Weak lensing surveys are often summarized by constraints on the derived parameter  $S_8 \equiv \sigma_8 \sqrt{\Omega_m}/0.3$ , obscuring the rich scale and redshift information encoded in the data, and limiting our ability to identify the origin of any tensions with  $\Lambda$ CDM predictions from the cosmic microwave background. In this work, we introduce a fast and flexible framework to extract the scale-dependent matter power spectrum  $P(k, z)$  from cosmic shear and CMB lensing measurements, parameterizing deviations from the *Planck*  $\Lambda$ CDM prediction as a free function  $\alpha(k)$ . Using public data from DES Y3, KiDS-1000, HSC Y3, and ACT DR6, we constrain  $\alpha(k)$  with fast Hamiltonian Monte Carlo inference, employing multipoles up to  $\ell_{\max} \sim 2000$  for the galaxy lensing surveys. Our results show a consistent 15–30% suppression in the matter power spectrum at intermediate scales ( $k \sim 0.1 \text{ Mpc}^{-1} - 1 \text{ Mpc}^{-1}$ ) in galaxy-lensing data relative to a *Planck*  $\Lambda$ CDM prediction with a CDM-only (no baryonic feedback) power spectrum, with combined tensions reaching up to  $4\sigma$ . This is under a fixed cosmology and with analytic marginalization over shear and redshift calibration uncertainties. In contrast, ACT CMB lensing is consistent with  $\Lambda$ CDM at  $k \lesssim 0.1 \text{ Mpc}^{-1}$ . We validate our method using mock data, quantify consistency between datasets, and demonstrate how the resulting  $\alpha(k)$  likelihoods can be used to test specific models for the power spectrum. All code, data products, and derived likelihoods are publicly released.<sup>a</sup> Our results highlight the importance of reporting lensing constraints on  $P(k, z)$  and pave the way for model-agnostic test of growth of structure with upcoming surveys such as LSST, *Euclid*, and *Roman*.

*Subject headings:* Weak gravitational lensing, large-scale structure, cosmological parameters

## 1. INTRODUCTION

Understanding the distribution of matter in the Universe is central to cosmology, and a range of observational probes allows us to study it. The cosmic microwave background (CMB) offers precise constraints on cosmological parameters, including the amplitude of matter fluctuations, denoted by  $\sigma_8$ . Meanwhile, weak lensing—whether of background galaxies or of the CMB itself—offers independent, direct measurements of the large-scale structure of the Universe. However, these methods are not in perfect agreement. Within the standard flat  $\Lambda$ CDM cosmological model, lensing measurements from galaxy surveys generally yield lower values of matter clustering than those inferred from CMB observations, including CMB lensing (Secco *et al.* 2022; Amon *et al.* 2022; Doux *et al.* 2022; Dalal *et al.* 2023; Asgari *et al.* 2021; Dark Energy Survey and Kilo-Degree Survey Collaboration *et al.* 2023; Madhavacheril *et al.* 2024; Qu *et al.* 2024; Planck Collaboration *et al.* 2020; Dalal *et al.* 2023; Wright *et al.* 2025). This tension is often summarized by the derived parameter  $S_8 \equiv \sigma_8 \sqrt{0.3/\Omega_m}$  (Secco *et al.* 2023), which captures a combination of fluctuation amplitude and matter density in the

parameter direction best constrained by galaxy weak-lensing experiments. While  $S_8$  provides a useful shorthand, it overlooks the fact that galaxy and CMB lensing probe different redshift ranges and physical scales (Tegmark and Zaldarriaga 2002). Consequently, the observed discrepancies could indicate new physics beyond the standard  $\Lambda$ CDM model. Therefore, a comprehensive analysis requires moving beyond the single parameter  $S_8$  and fully exploiting the rich information contained within these datasets.

To do so, here we directly reconstruct the matter power spectrum  $P(k, z)$  using galaxy and CMB lensing data. This spectrum encodes the statistical distribution of matter across different scales and redshifts and is a fundamental prediction of cosmological models computed by established Boltzmann solvers like CLASS (Lesgourgues 2011) and CAMB (Lewis *et al.* 2000). Using publicly-available galaxy-lensing data from the Dark Energy Survey (DES, The Dark Energy Survey Collaboration 2005), the Kilo Degree Survey (KiDS, de Jong *et al.* 2013), and Hyper Suprime-Cam (HSC) Subaru Strategic Program (Aihara *et al.* 2018), combined with CMB-lensing data from the Atacama Cosmology Telescope (ACT, Swetz *et al.* 2011), we infer scale-dependent deviations from the matter power spectrum predicted by the best-fit *Planck*  $\Lambda$ CDM model (Planck Collaboration *et al.* 2020).

Our approach introduces a linearized parameterization of these deviations, enabling a fast and flexible exploration

doux@lpsc.in2p3.fr  
karwal@uchicago.edu

<sup>a</sup> The code, data, intermediate and final results, as well as a reproducible notebook for further model testing, are available in the GitHub repository: <https://github.com/xuod/cls2pk>.

of the matter power spectrum inferred from lensing data, bridging the gap between observations and theory. Importantly, we do not assume any specific physical origins for the deviations—whether they result from baryonic effects, intrinsic alignments, nonlinear structure formation, or genuinely new physics. Rather, we aim to characterize their presence and scale-dependence directly from the data.

Recent studies have explored modifications to the cold dark matter power spectrum as a potential solution to the apparent  $S_8$  tension. These approaches include empirically parameterizing a suppression of power on small scales (Amon and Efstathiou 2022; Preston *et al.* 2023; Broxterman and Kuijken 2024) or at late times (Abbott *et al.* 2023; Lin *et al.* 2024), modeling baryonic feedback mechanisms (Terasawa *et al.* 2025), introducing dark matter interactions (Preston *et al.* 2025; Zhou and Weiner 2024; Khoury *et al.* 2025; Poulin *et al.* 2023; Asghari *et al.* 2019; Beltrán Jiménez *et al.* 2021), using perturbative expansions (Ye *et al.* 2024), and employing alternative reconstruction techniques (Preston *et al.* 2024; Simon *et al.* 2025; Perez Sarmiento *et al.* 2025). Our method complements these efforts by offering a heuristic yet data-driven framework for testing consistency with  $\Lambda$ CDM.

Our inference approach is presented in Section 2. Details of the datasets are provided in Section 3. Our methodology—including binning choices, treatment of systematics, and validation with mock data—is described in Section 4. Our main results, quantifying individual and combined deviations of the lensing datasets from  $\Lambda$ CDM cosmology, are presented in Section 5. Section 6 outlines the scope and potential applications of these results, demonstrating how this approach can be used to constrain physics beyond  $\Lambda$ CDM, with concrete examples based on two different prescriptions for the small-scale power spectrum. Finally, we conclude with a summary of our findings and our outlook in Section 7.

All code, intermediate data products, and posterior samples of  $\alpha(k)$  used in this work are publicly available at <https://github.com/xuod/cls2pk>. We encourage lensing surveys to present similar constraints on the matter power spectrum  $P(k, z)$ , moving beyond the traditional  $S_8$  summary statistic. In addition, we provide ready-to-use tools for theorists to test the viability of their models against the reconstructed  $\alpha(k)$ , capturing the scale-dependence of deviations. These are packaged as modular likelihoods compatible with MontePython (Audren *et al.* 2013), enabling fast and flexible model comparison.

## 2. FAST POWER SPECTRUM INFERENCE

The galaxy and CMB lensing power spectra  $C_\ell$  can be computed as line-of-sight integrals over the matter power spectrum  $P(k, z)$  weighted by specific window functions. Within the Limber approximation (LoVerde and Afshordi 2008; Mandelbaum 2018), this relationship is given by

$$C_\ell^{ab} = \int d\chi \frac{q_a(\chi)q_b(\chi)}{\chi^2} P\left(k = \frac{\ell + 1/2}{\chi}, z(\chi)\right), \quad (1)$$

where  $\chi$  is the radial comoving distance from the observer, and the window functions  $q_a$  encode information about the sources and cosmic distances. For CMB lensing, this window function is

$$q_a(\chi) = \frac{3\Omega_m H_0^2}{2c^2} \frac{\chi}{a(\chi)} \frac{\chi - \chi_*}{\chi_*}, \quad (2)$$

where  $\chi_*$  is the comoving distance to the surface of last scattering and  $a$  is the scale factor. For galaxy lensing, it becomes

$$q_a(\chi) = \frac{3\Omega_m H_0^2}{2c^2} \frac{\chi}{a(\chi)} \int_\chi^{\chi_*} d\chi' n_a(\chi') \frac{\chi - \chi'}{\chi'}, \quad (3)$$

where  $n_a(\chi)$  is the redshift distribution of the  $a$ -th tomographic bin of source galaxies.

We introduce a scale-dependent, redshift-independent modulation  $\alpha(k)$  of the matter power spectrum given by

$$P(k, z) = [1 + \alpha(k)] P_{\text{fid}}(k, z), \quad (4)$$

where  $P_{\text{fid}}(k, z)$  is the nonlinear matter power spectrum computed using the *Planck* best-fit  $\Lambda$ CDM cosmology (Planck Collaboration *et al.* 2020), employing the standard halo fit prescription for nonlinearities (Takahashi *et al.* 2012). By changing the integration variable in Eq. (1) from  $\chi$  to  $k = (\ell + 1/2)/\chi$  and then to  $\log k$ , this linear relation can be discretized into a sum over  $n_k$  logarithmically-spaced  $k$ -bins with centers  $\log k_i$  and width  $\Delta_{\log k}$ . Given a vector  $\mathbf{C}^{ab}$  of length  $n_\ell$  representing measurements of angular power spectra for tomographic bins  $a$  and  $b$  over a range of multipoles  $\ell$ , we obtain a linear model

$$\mathbf{C}^{ab} = \mathbf{W}^{ab} (\mathbf{1} + \boldsymbol{\alpha}), \quad (5)$$

where  $\boldsymbol{\alpha} = (\alpha(k_1), \dots, \alpha(k_{n_k}))$  represents deviations introduced in Eq. (4),  $\mathbf{1} = (1, \dots, 1)$  is a vector of ones, and the window matrix  $\mathbf{W}^{ab}$  has  $n_\ell \times n_k$  elements given by

$$\mathbf{W}_{\ell, k_i}^{ab} = \Delta_{\log k} \frac{q_a(\chi_\ell^i) q_b(\chi_\ell^i)}{\chi_\ell^i} P_{\text{fid}}(k_i, z(\chi_\ell^i)), \quad (6)$$

with  $\chi_\ell^i = (\ell + 1/2)/k_i$ . We then stack vectors and window matrices for every tomographic bin combination  $ab$ , and potentially for multiple data sets to combine them. To account for the fact that power spectra are measured in multipole bins (or bandpowers), we convolve the window matrices in Eq. (6) by the corresponding binning matrices (Alonso *et al.* 2019; Nicola *et al.* 2021), such that the model remains linear, as in Eq. (5).

The likelihoods for the galaxy- and CMB-lensing datasets used here are multivariate Gaussian distributions with fixed covariance matrices. Therefore, at fixed cosmology,  $\mathbf{W}$  is a constant matrix and using Eq. (5) to compute the means of these likelihoods results in the following statistical model

$$\mathcal{L}(\mathbf{C}|\boldsymbol{\alpha}) = \mathcal{N}(\mathbf{C}; \mathbf{W}(\mathbf{1} + \boldsymbol{\alpha}), \boldsymbol{\Sigma}), \quad (7)$$

where  $\mathbf{C}$  is the stacked data vector,  $\mathbf{W}$  the corresponding stacked window matrix, and  $\boldsymbol{\Sigma}$  the data covariance. This constitutes a differentiable model suitable for efficient Bayesian sampling using Hamiltonian Monte-Carlo techniques implemented in probabilistic programming libraries such as PyMC (Abril-Pla *et al.* 2023).

We note that Tegmark and Zaldarriaga (2002) proposed a direct, analytic inversion of Eq. (5) that was used *e.g.* in Doux *et al.* (2022). However, it requires a strong regularization for  $k$ -modes that are not well-constrained by the data, adding a hyperparameter that depends on the choice of binning, and potentially leading to numerical instabilities—at least for the specific exercise at hand. In contrast, with a Bayesian inversion, poorly constrained  $k$ -modes are simply prior-dominated, independent of binning.

## 3. DATA

## 3.1. Weak-lensing survey data

## 3.1.1. Data sets

Our analysis incorporates public data from three galaxy weak-lensing surveys and their recent cosmic shear analyses: DES Year 3<sup>1</sup> (DES Y3, Doux *et al.* 2022), KiDS-1000<sup>2</sup> (Asgari *et al.* 2021), and HSC Year 3<sup>3</sup> (HSC Y3, Dalal *et al.* 2023). From each survey, we use only the cosmic shear data, which includes the source redshift distributions  $n_a(z)$  of the tomographic bins of source galaxies, the auto- and cross-correlated shear power spectra  $C_\ell^{ab}$  between these bins, and their covariance matrices. DES Y3 has 4 tomographic bins, hence 10 cross-correlation combinations for shear power spectra, as does HSC Y3. KiDS-1000 has 5 tomographic bins for the redshift distributions of their sources and hence 15 combinations of these bins.

For DES and KiDS, we use the entire range of scales available in measured power spectra, with  $\ell_{\max} \approx 2000$ . HSC probes at far greater angular resolution, and we present results here making the scale cuts  $300 < \ell < 1800$  recommended by their main analysis (Dalal *et al.* 2023) as well as a separate analysis including all scales up to  $\ell_{\max} \approx 15800$  (see Section 7). Note that these extremely small scales extend beyond the range where cosmological modeling is reliable due to uncertainties from baryonic effects and nonlinear evolution. Regardless, we include them in Section 7 to explore how the data itself constrains this regime of the projected power spectrum but caution against interpreting it for cosmological inference.

## 3.1.2. Marginalization over systematic effects

For all three surveys, we include uncertainties  $\Delta z_a$  in the redshift distributions  $n_a(z)$  of source galaxies

$$n_a(z) \rightarrow n_a(z + \Delta z_a), \quad (8)$$

where  $z = z(\chi)$  as before. This allows for a translation in redshift of the entire redshift distribution of bin  $a$ . Here  $\Delta z_a$  have Gaussian priors following the recommendations from each experiment, except for the last two redshift bins for HSC.<sup>4</sup> For these bins, the original analysis posits that the source redshift calibrations are inaccurate, assumed to be shifted by a Gaussian with a mean and error that is marginalized over. Here, we adopt the posteriors of that marginalization as our priors for these two bins. This remains a conservative choice as the original analysis arrived at the posteriors while simultaneously marginalizing over cosmology, while we fix our cosmology to *Planck*  $\Lambda$ CDM.

For HSC and DES, we also include uncertainties  $m_a$  in the shear calibration of each bin such that the overall shear amplitude of the bin can be rescaled as

$$C_\ell^{ab} \rightarrow (1 + m_a)(1 + m_b)C_\ell^{ab}. \quad (9)$$

<sup>1</sup> DES Year 3 catalogs and real-space measurements are publicly available from *NCSA*. Harmonic-space measurements used here are available upon request to Cyrille Doux.

<sup>2</sup> KiDS-1000 data are publicly available from the *KiDS* website.

<sup>3</sup> HSC Year 3 data were provided by Roohi Dalal.

<sup>4</sup> For DES Y3, the priors are provided in Table 1 of Doux *et al.* (2022). For KiDS-1000, we use means and standard deviations from Table 1 of Asgari *et al.* (2021) and the correlation matrix shown in Fig. 6 of Hildebrandt *et al.* (2021) to compute the correlated prior. For HSC Y3, priors are given in Table 1 of Dalal *et al.* (2023). For bins 3 and 4, the prior is uniform in the range  $[-1, +1]$ , and we instead use the redshift parameter posteriors from Table VI.

TABLE 1

EFFECTIVE SCALES AND REDSHIFTS PROBED BY THE FOUR LENSING SURVEYS CONSIDERED IN THIS WORK. THEY ARE COMPUTED AS THE MEANS OF THE DISTRIBUTIONS OF THEIR SIGNAL-TO-NOISE RATIO IN  $(k, z)$  SPACE, DEFINED IN EQ. (12).

Experiment	$k_{\text{eff}}$	$z_{\text{eff}}$
DES Y3	$2.6 \times 10^{-1} \text{ Mpc}^{-1}$	0.36
KiDS-1000	$3.2 \times 10^{-1} \text{ Mpc}^{-1}$	0.37
HSC Y3	$5.1 \times 10^{-1} \text{ Mpc}^{-1}$	0.49
ACT DR6	$3.5 \times 10^{-2} \text{ Mpc}^{-1}$	2.08

These are assumed to be redshift independent within each bin following the analyses of the surveys, and we again adopt the Gaussian priors on these systematic parameters prescribed by the surveys. For KiDS, shear biases are included in the data covariances so we do not vary  $m_a$  as additional parameters, following their analysis (Joachimi *et al.* 2021).

To account for these uncertainties, we analytically marginalize over these biases, assuming Gaussian priors, following the method described in Bridle *et al.* (2002); Taylor and Kitching (2010). In essence, it adds a term to the data covariance matrix  $\Sigma$  such that

$$\Sigma \rightarrow \Sigma + \sum_{\theta} \sigma_{\theta}^2 \partial_{\theta} C^{ab} \cdot \partial_{\theta} C^{ab\text{T}}, \quad (10)$$

where the sum runs over the parameters  $\theta$  to be marginalized over,  $\sigma_{\theta}$  is the standard deviation of the prior<sup>5</sup> and  $\partial_{\theta} C^{ab}$  is the partial derivative of the shear power spectrum data vector with respect to  $\theta$ , which we evaluate analytically for shear biases and numerically for redshift distributions. Note that we estimate this extra covariance term as well as window matrices at the mean of the priors.

We do not include intrinsic alignment or baryonic effects in our treatment of systematics for any of the surveys in our analysis. Indeed, both will affect the projected power spectrum probed by weak-lensing surveys, which we attempt to reconstruct rather than model explicitly (see Section 5).

## 3.2. CMB lensing

We use ACT DR6 data<sup>6</sup>, the provided data covariance and follow their binning scheme for the CMB lensing power spectrum  $C_\ell$  (Qu *et al.* 2024; Madhavacheril *et al.* 2024). We include multipoles in the range  $40 < \ell < 763$ , following the ACT DR6 analysis (see Section 6.1 of Qu *et al.* (2024)). The CMB lensing power spectrum has no systematics beyond astrophysical foregrounds, which are already accounted for in the provided covariance matrix.

3.3. Sensitivity of data on the  $(k, z)$  plane

Each galaxy-lensing survey has different sky footprints, survey areas, depths and tomographic redshift bins. CMB lensing has a different window function entirely. They each hence probe cosmology at different scales and redshifts. We delineate the sensitivity of each survey on the  $(k, z)$  plane in Fig. 1. This is determined by calculating

$$\frac{\partial^2 C_\ell^{ab}}{\partial \log k \partial z} = \frac{q_a(\chi)q_b(\chi)}{\chi} P(k, z(\chi)) \delta\left(k = \frac{\ell + 1/2}{\chi}\right) \quad (11)$$

<sup>5</sup> For KiDS, the redshift calibration errors are correlated, and  $\sigma_{\theta}$  is straightforwardly promoted to a covariance matrix  $\Sigma_{\theta}$ .

<sup>6</sup> ACT DR6 CMB lensing data is publicly available from *LAMBDA*.

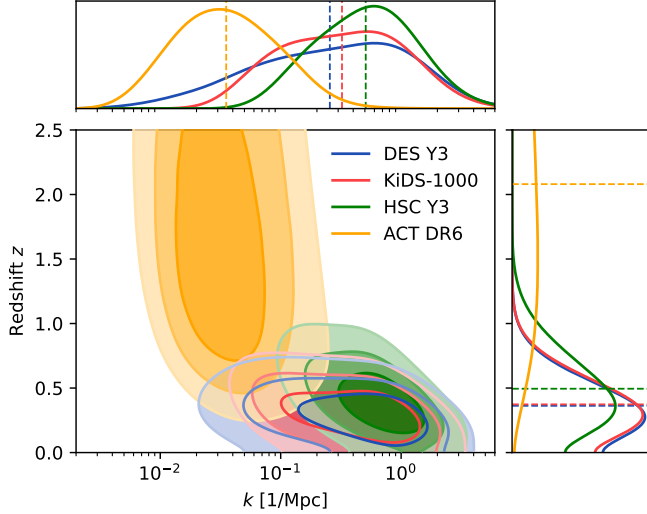


Fig. 1.— The contours in the main panel show the signal-to-noise ratio (SNR) defined in Eq. (12) and hence the sensitivity of each experiment on the scale-redshift  $(k, z)$  plane. The upper and right panels show the SNR projected along each direction, with dashed lines denoting the mean redshifts and (log) scales that the experiments are sensitive to (mean values are provided in Table 1). Where the contours overlap, they probe the same physics in redshift-independent  $\alpha(k)$ . However, as CMB- and galaxy-lensing surveys have little overlap, there are conceivable models that may impact the  $P(k, z)$  probed by one observable but not the other. Therefore, we urge caution when combining these data sets on  $P(k, z)$  and  $\alpha(k)$ . The HSC contours exclude scales following the original HSC analysis, such that all galaxy surveys have  $\ell_{\max} \approx 2000$ . When including all HSC scales, the sensitivity extends to smaller scales, as expected. We also account for the ACT fiducial scale cuts, with  $\ell_{\max} = 763$ . Note that the contours are simply linearly spaced from the maximum SNR to 0, these do not represent  $\sigma$  levels.

for each tomographic bin pair and stacking them. We then take the resultant vector  $\partial_{\log k z}^2 \mathbf{C}$  and compute the signal-to-noise ratio (SNR) as

$$\text{SNR}(\log k, z) = \sqrt{\partial_{\log k z}^2 \mathbf{C} \cdot \boldsymbol{\Sigma}^{-1} \cdot \partial_{\log k z}^2 \mathbf{C}^T}, \quad (12)$$

where  $\boldsymbol{\Sigma}$  is the covariance of the  $C_\ell^{ab}$  including systematics.

Because the Limber relation  $k = (\ell + 1/2)/\chi(z)$  links angular multipoles to physical wavenumbers, each multipole  $\ell$  samples a slice in the  $(k, z)$  plane. When combined across multipoles and tomographic bins, the surveys accumulate sensitivity through this plane, as shown in Fig. 1. Table 1 indicates the corresponding effective scales and redshifts of peak sensitivity for each experiment. As a consequence, while a scale-dependent modification such as  $\alpha(k)$  is formally a function of  $k$  alone, constraints on  $\alpha(k)$  at different wavenumbers are informed by different redshift ranges. This redshift dependence arises from the survey geometry and window functions, rather than from the theoretical definition of  $\alpha(k)$  itself.

DES and KiDS almost completely overlap, and share a significant overlap with HSC, which is a deeper survey and hence probes slightly higher redshifts. The survey area for HSC is smaller, hence the compression of its contour towards smaller scales and larger  $k$ . However, galaxy-lensing sensitivity has little overlap with CMB lensing. The CMB-lensing kernel peaks at  $z \approx 2$ , while all galaxy lensing kernels peak at  $z \lesssim 1$ , leading to minimal redshift overlap. These hence also probe physics at different scales, with CMB lensing probing entirely linear scales and galaxy lensing extending into quasi-linear and nonlinear scales. For this reason, we will refrain from claiming a reconstruction of the present-day matter power

TABLE 2  
FIDUCIAL COSMOLOGICAL PARAMETERS FROM *Planck* 2018  
(TT,TE,EE+LOWE) USED IN THIS WORK.

Parameter ([unit])	Value
$\Omega_b h^2$	0.02236
$\Omega_c h^2$	0.1202
$\ln(10^{10} A_s)$	3.045
$n_s$	0.9649
$H_0$ [km/s/Mpc]	67.27
$N_{\text{eff}}$	3.046
$m_\nu$ [eV]	0.06 (1 massive, 2 massless)

spectrum,  $P(k, z = 0)$ , and focus on our specific, yet general, scale-dependent parametrization via  $\alpha(k)$  of  $P(k, z)$ .

### 3.4. Survey correlations

Whenever possible, we aim to combine data sets to tighten constraints on  $\alpha(k)$ . Given the overlap in  $(k, z)$  space and on the sky, we account for correlations between the experiments with an approximate cross-covariance. To do so, we start from the analytic expression for the unbinned spectra (García-García *et al.* 2019; Friedrich *et al.* 2021)

$$\text{Cov}\left(C_\ell^{ab}, C_{\ell'}^{a'b'}\right) \approx \delta_{\ell\ell'} \frac{C_\ell^{aa'} C_\ell^{bb'} + C_\ell^{ab'} C_\ell^{ba'}}{(2\ell + 1)} \frac{f_{\text{sky}}^{\text{overlap}}}{f_{\text{sky}} f_{\text{sky}}'}, \quad (13)$$

where  $f_{\text{sky}}$  and  $f_{\text{sky}}'$  are the respective sky fractions of the surveys being correlated, and  $f_{\text{sky}}^{\text{overlap}}$  the sky fraction of their overlap. We amended the formula from García-García *et al.* (2019); Friedrich *et al.* (2021), which has a term  $1/f_{\text{sky}}$  instead of the ratio we propose, to account for the fact that for fixed survey areas, the cross-covariance reduces if the overlap decreases. We then finally convolve this expression with the binning window matrices.

While this is an approximation, the overlap on sky is generally small—except when combining galaxy surveys with CMB lensing data, in which case the overlap in  $(k, z)$  space becomes small—meaning that cross-covariance should be relatively small and only have a minor impact on  $\alpha(k)$  constraints. In practice, we find that neglecting this cross-covariance shifts the  $\alpha(k)$  tension by less than  $0.1 \sigma$  (see definitions in the next section and column  $n_\sigma$  of Table 3), validating our approach.

## 4. IMPLEMENTATION AND VALIDATION

Our analysis adopts the *Planck* 2018 cosmology (Planck Collaboration *et al.* 2020) (TT,TE,EE+lowE) as the fiducial model. The parameters are listed in Table 2. We assume one massive neutrino with mass  $m_\nu = 0.06$  eV, two massless species, and  $N_{\text{eff}} = 3.046$ . All cosmological quantities are computed using the Core Cosmology Library (CCL, Chisari *et al.* 2019).

### 4.1. Binning and smoothing

For our analysis to be reasonably accurate, the model in Eq. (5) must approximate the full Limber integral in Eq. (1) to a fraction of the error bars. Therefore, the  $k$ -bins must cover the full range of  $k$ -modes that contribute to the signal for all measurements, and be sufficiently thin. In practice, we find that these conditions are reached for all surveys for  $n_k \gtrsim 20$  logarithmically-spaced bins in the range  $10^{-3} \text{ Mpc}^{-1}$  to  $10^2 \text{ Mpc}^{-1}$ , which we fix at  $n_k = 24$  throughout this work.

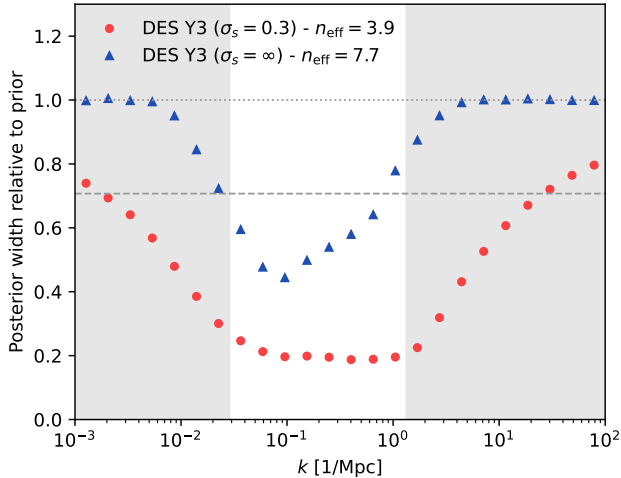


FIG. 2.— Ratios of the posterior and prior widths for  $\alpha(k)$  for DES using  $n_k = 24$   $k$ -bins, without (blue triangles) and with (red points) a smoothing prior. From the case without smoothing, we can determine the  $k$ -range that is constrained  $\sim 3 \times 10^{-2} \text{ Mpc}^{-1} < k < 1 \text{ Mpc}^{-1}$  shown by the unshaded band between the gray areas. We use the prior and posterior covariances to compute the effective number of constrained parameters, of order  $n_{\text{eff}} \approx 6.5$  for DES, on par with the 9 bins in the constrained range. Smoothing reduces the relative impact of data and the effective number of constrained bins to  $n_{\text{eff}} \approx 4.0$ , but yields more physical curves.

Another sensible requirement to ease the interpretation of our results is to choose  $n_k$  such that the number of  $k$ -bins in the range that is constrained by the data (see Fig. 1) does not greatly exceed the effective number of modes that are actually constrained by the data. To do so, we performed tests varying this value and comparing the width of the posterior to that of the  $[-1, +1]$  uniform prior, as shown on Fig. 2. We find that  $n_k = 24$  allows us to meet this requirement as well.

Undesirably, adjacent  $k$ -bins are strongly anticorrelated in this configuration. This is evident in the leftmost panel of Fig. 3 showing the correlation matrix of the posterior distribution, determined using a Gaussian likelihood with the model in Eq. (5), the data covariance plus the systematics marginalization term, and a uniform prior in the range  $[-1, +1]$ . This is expected, as adjacent bins may compensate each other in Eq. (5), allowing oscillating patterns. However, such patterns may be unphysical and they limit the interpretability of our results.

We therefore enforce a certain level of smoothness on the reconstructed  $\alpha(k)$ , penalizing rapid variations while avoiding biasing the reconstruction towards the fiducial  $\Lambda$ CDM model, loosely inspired by Raveri (2020). To do so, we impose a Gaussian prior  $\Pi_s(\alpha)$  on the differences of adjacent  $\alpha(k)$ 's

$$\Pi_s(\alpha) = \prod_{i=1}^{n_k-1} \mathcal{N}(\alpha(k_{i+1}) - \alpha(k_i); 0, \Delta_{\log k} \sigma_s). \quad (14)$$

The coefficient  $\sigma_s$  allows us to vary the constraint on the derivative of the reconstructed  $\alpha(k)$ , such that  $|\Delta\alpha/\Delta_{\log k}| \lesssim \sigma_s$ . This setup then allows smooth deviations from the fiducial  $\Lambda$ CDM but suppresses rapid oscillations between adjacent bins, decorrelating them.

We adopt a heuristic approach to choose  $\sigma_s$ , picking the value that approximately decorrelates adjacent bins. In other words, we balance the data and prior such that variations in  $\alpha(k)$  are roughly independent in the posterior distribution, allowing one to read “ $\chi$ -by-eye” on plots, at the price of reducing

the effective number  $n_{\text{eff}}$  of constrained parameters. For the covariance matrices of the prior  $C_{\Pi_s}$  and the posterior  $C_p$ , this can be estimated as

$$n_{\text{eff}} = \text{Tr}\left(\mathbb{I} - C_{\Pi_s}^{-1} C_p\right) = n_k - \text{Tr}\left(C_{\Pi_s}^{-1} C_p\right), \quad (15)$$

where  $\text{Tr}$  is the trace operator (Raveri et al. 2020). For DES, we find  $n_{\text{eff}} \approx 7.8$  without a smoothing prior (corresponding to  $\sigma_s = \infty$ ), and  $n_{\text{eff}} \approx 3.6$  with a smoothing prior of strength  $\sigma_s = 0.3$  that yields an approximately diagonal posterior in the constrained  $k$ -range.

With these choices for  $n_k = 24$  bins and smoothing scales  $\sigma_s = \{0.3, \infty\}$ , we use Eq. (5) to obtain constraints on  $\alpha(k)$  through Hamiltonian Monte Carlo sampling using the PyMC package. While the smoothed  $\alpha(k)$  form our main results, the unsmoothed  $\alpha(k)$  help determine the scales for which  $\alpha$  is constrained over its prior, as illustrated by the unshaded region in Fig. 2. This range is determined by selecting bins in which the variance of the posterior distribution is less than half that of the prior (which is  $1/3$  for a uniform prior over  $[-1, +1]$ ), and the number of constrained bins  $\tilde{n}_k$  are reported in Table 3 for all data combinations. In practice, we find that this range captures roughly 90% of the total constraining power estimated with Eq. (15).

#### 4.2. Recovery of deviations

In this section, we validate that our approach can recover injected deviations from  $\Lambda$ CDM. To do so, we employ the DES setup, but use data vectors computed with the full Limber equation (see Eq. (1)) for three specific models. We employ the scalar  $A_{\text{mod}}$  parametrization suggested in Amon and Efstathiou (2022) to model deviations from the standard power spectrum as a function of the linear  $P_{\text{lin}}$  and nonlinear power spectra  $P_{\text{nl}}$  given by

$$P(k, z) = P_{\text{lin}}(k, z) + A_{\text{mod}}(P_{\text{nl}}(k, z) - P_{\text{lin}}(k, z)). \quad (16)$$

In our next test, we vary the prescription for the nonlinear power spectrum and use HMCode (Mead et al. 2021) to compute a power spectrum that includes a model for baryonic effects that suppress fluctuations around  $k \sim 1 \text{ Mpc}^{-1}$  and enhances them on smaller scales. In this model, a higher AGN temperature  $T_{\text{AGN}}$  causes less power suppression because the more energetic feedback ejects gas farther from halos, reducing its long-term impact on suppressing small-scale matter clustering. Finally, we test a scale-dependent modified-gravity model with the  $(\Sigma, \mu)$  parametrization, which differentiates the gravitational potentials experienced by matter and by light, with values  $\Sigma_0 = 0$ ,  $\mu_0 = 0.5$  and  $c_1^H = 2$  as implemented in CCL (Chisari et al. 2019).

The results shown in Fig. 4 demonstrate that our method recovers the input deviations in the  $k$ -range that is constrained by the data. The red lines show the relative differences between the tested power spectrum model and the fiducial one, evaluated at both redshift  $z = 0$  and at the effective DES redshift,  $z_{\text{eff}} = 0.36$ . Posterior distributions are represented by boxes with vertical extent showing the 68% limits on  $\alpha(k)$  components computed with GetDist (Lewis 2019), and horizontal extent showing the width of the  $k$ -bins. Importantly, our model is only scale-dependent, such that if a deviation is also redshift-dependent, we will only recover the scale-dependent part at an effective redshift probed by the data. This is illustrated in the lowest panel for the modified-gravity case, where we recover the deviations not at  $z = 0$ , but at the approximate effective redshift  $z \approx 0.36$  probed by DES data, as illustrated in

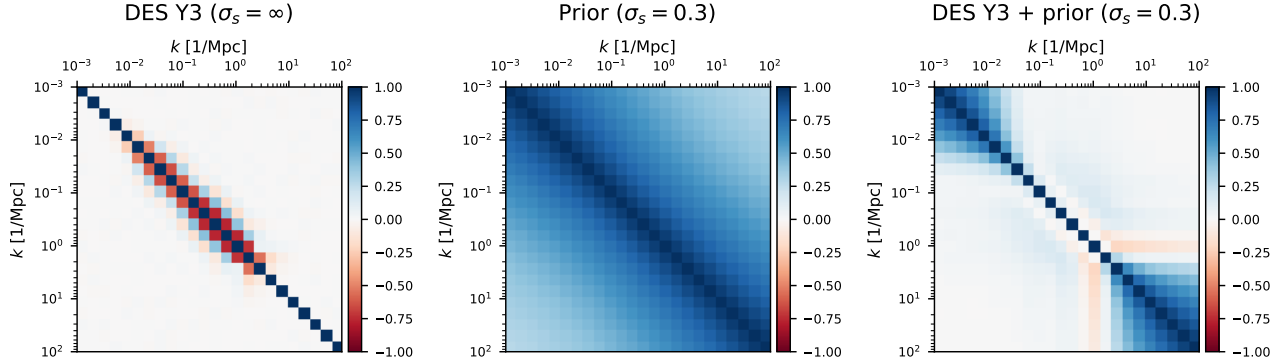


FIG. 3.— Correlation matrices of the posterior distribution of  $\alpha$ 's for DES without smoothing (left), of the smoothing prior with smoothing strength  $\sigma_s = 0.3$  (center), and of the posterior distribution for DES when including this smoothing prior (right). The middle and right panels demonstrate the strong correlations introduced across bins where data loses sensitivity at small and large  $k$ , in the regions beyond where  $\alpha(k)$  are well-constrained.

Fig. 1. The smoothing prior is also shown in Fig. 4 through the comparison of smoothed and unsmoothed posteriors. It regularizes the reconstruction by damping oscillations between adjacent  $k$ -bins, as motivated in Section 4.1. This prior leaves the posterior mean unchanged but reduces bin-to-bin correlations, tightening the marginalized constraints.

## 5. RESULTS

### 5.1. Constraints from individual surveys

Figure 5 shows the constraints on  $\alpha(k)$  obtained from each lensing survey independently. We report constraints for  $n_k = 24$  logarithmically spaced  $k$ -bins in the range  $10^{-3} \text{ Mpc}^{-1}$  to  $10^2 \text{ Mpc}^{-1}$ , with and without a smoothing prior of strength  $\sigma_s = 0.3$ , as per Eq. (14). These deviations should only be noted in the regions where surveys actually constrain the matter power spectrum (see Figs. 1 and 2). Outside these regions, in the gray bands,  $\alpha(k)$  is unconstrained and a model need not have zero deviation from  $\Lambda$ CDM to fit data. Also note that the regions are different for every survey, particularly between galaxy and CMB lensing surveys.

Notably, all three galaxy lensing surveys find similar suppression in  $\alpha(k)$  in their individual constrained regions. We find that these data favor a 15-to-30% suppression of the matter power spectrum in the range  $k \sim 0.1 \text{ Mpc}^{-1} - 1 \text{ Mpc}^{-1}$  than extrapolated from *Planck* CMB observations at high redshift, in agreement with constraints reported by galaxy surveys (Doux *et al.* 2022; Dalal *et al.* 2023; Asgari *et al.* 2021). Section 7 illustrates the robustness of these constraints when systematics marginalization is ignored, or using less conservative scale cuts.

These results are quantified in Table 3. We report the level of tension between the  $\alpha(k)$  constraints and their fiducial zero-value if agreement with *Planck* was perfect, computing a  $\Delta\chi^2_\alpha$  using the mean and covariance of the sample, excluding the gray regions in  $k$  where each individual experiment loses sensitivity as shown in Fig. 5. Given the probability  $p$  to exceed the observed value, its significance is given in units of Gaussian standard deviations by  $n_\sigma = \sqrt{2} \text{erf}^{-1}(1 - p)$ , and we consider that there is no significant tension for  $p > 0.01$ , corresponding to  $n_\sigma < 2.6\sigma$ . Using this metric, we find that DES and HSC have a mild tension (below  $3\sigma$ ) with the fiducial model, while ACT is in excellent agreement. KiDS seems to strongly reject *Planck*  $\Lambda$ CDM, with the caveat that our model itself provides a poor fit to KiDS data (see below).

The posterior uncertainties shown here are evaluated at fixed *Planck*  $\Lambda$ CDM cosmological parameters. While one could in

principle propagate the *Planck* parameter uncertainties into  $\alpha(k)$ , these are significantly smaller than the constraints from the lensing surveys themselves. Including this effect would therefore lead to only a subdominant broadening of the inferred posteriors and would not qualitatively change the tension levels quoted in Table 3. For completeness, we repeat the inference with the DES Y3 harmonic-space cosmology (Doux *et al.* 2022) as fiducial; Section 7 shows that beyond an expected overall amplitude shift, the scale dependence within the constrained  $k$ -range is very similar. A full accounting of parametric uncertainties in the chosen fiducial cosmology is beyond the scope of this paper.

Table 3 also provides the goodness-of-fit of the model described by Eq. (5), and its significance computed with a number of degrees of freedom given by the data-vector size minus the effective number  $n_{\text{eff}}$  of constrained bins from Eq. (15). We find that our linear model generally provides a good fit to data, except for KiDS-1000. The best-fit of our model  $n_\sigma \approx 2.7\sigma$  is only marginally worse than the one reported in Asgari *et al.* (2021) with a  $p$ -value of 0.013, corresponding to  $n_\sigma \approx 2.5\sigma$ .<sup>7</sup> This poor fit may be indicative of a tension requiring a redshift-dependent model, unlike the one used here, or systematic effects that are not accounted for. We also note that recent results from the complete KiDS-Legacy dataset, with improved redshift calibration, show better internal consistency and are in agreement with *Planck* (Wright *et al.* 2025), supporting the need for a redshift-dependent model.

We reiterate that these  $\alpha(k)$  denote all departures not just from  $\Lambda$ CDM, but specifically from the assumption that lensing surveys measure the projected  $\Lambda$ CDM nonlinear matter power spectrum computed at *Planck* cosmology with *halofit*. An overall suppression in the matter power spectrum therefore need not arise from new physics exclusively, but can also be explained by shifts in  $\Lambda$ CDM parameters relative to *Planck*, or by contributions from intrinsic alignments and baryonic feedback that impact weak-lensing surveys. In particular, KiDS-1000 reported a  $2.5\sigma$  detection (for shear bandpowers) of redshift-independent intrinsic alignments with an amplitude  $A_{\text{IA}} \sim 1$  that suppress power on all scales. When including this contribution in the Limber approximation and window matrices using a redshift-independent nonlinear alignment model (NLA, Hirata and Seljak 2004; Bridle and King 2007) with an amplitude of  $A_{\text{IA}} = 1$ , the tension reduces from  $4.8\sigma$  to  $3.7\sigma$  for KiDS-1000, without any marginalization, close to the  $3.4\sigma$

<sup>7</sup> Removing bin 2 which was found to be inconsistent with the others bins, albeit with negligible impact on cosmology, does not help to improve the fit.

TABLE 3

Comparison of  $\alpha(k)$  posteriors using a fiducial *Planck*  $\Lambda$ CDM power spectrum, excluding intrinsic alignments and baryonic feedback. The columns show: (1) the datasets used; (2) the number of  $C_\ell$  data points; (3) the number  $\bar{n}_k$  of constrained  $k$ -bins; (4) the smoothing level  $\sigma_s$  (see Section 4 for definitions of  $\bar{n}_k$  and smoothing); (5) the  $\Delta\chi_\alpha^2$  computed using only the constrained  $k$ -bins, and (6) the significance  $n_\sigma$  of the tension with *Planck* in the  $\alpha(k)$  projection; and the goodness-of-fit of our linear model, including (7) the  $\chi_{\min}^2$  at the best-fit, (8) the effective number  $n_{\text{eff}}$  of constrained parameters (see Eq. (15)), and (9) the significance  $n_\sigma$  of the deviation in Gaussian standard deviations. We note that poor fits ( $n_\sigma \gtrsim 2.5 \sigma$ ) in the last column may indicate that our redshift-independent model is insufficient to describe the data, that data favor different  $\Lambda$ CDM parameters, or the presence of unknown systematic effects.

Data combination	Data points	$\bar{n}_k$	Smoothing	$\alpha(k)$ tension		Goodness-of-fit		
				$\Delta\chi_\alpha^2$	$n_\sigma$	$\chi_{\min}^2$	$n_{\text{eff}}$	$n_\sigma$
DES Y3	320	8	$\sigma_s = \infty$	34.8	4.2 $\sigma$	346.7	7.7	1.7 $\sigma$
			$\sigma_s = 0.3$	23.9	3.0 $\sigma$	351.5	3.9	1.7 $\sigma$
HSC Y3	60	5	$\sigma_s = \infty$	10.7	1.9 $\sigma$	60.3	4.9	1.0 $\sigma$
			$\sigma_s = 0.3$	14.4	2.5 $\sigma$	60.5	2.5	0.9 $\sigma$
KiDS-1000	120	7	$\sigma_s = \infty$	37.4	4.6 $\sigma$	156.7	5.1	2.8 $\sigma$
			$\sigma_s = 0.3$	42.0	5.0 $\sigma$	159.4	2.4	2.7 $\sigma$
ACT DR6	10	6	$\sigma_s = \infty$	10.4	1.6 $\sigma$	4.0	4.7	0.5 $\sigma$
			$\sigma_s = 0.3$	2.9	0.2 $\sigma$	6.6	2.2	0.6 $\sigma$
DES+HSC	380	8	$\sigma_s = \infty$	39.6	4.6 $\sigma$	416.7	8.4	1.9 $\sigma$
			$\sigma_s = 0.3$	37.1	4.4 $\sigma$	419.4	4.4	1.9 $\sigma$
DES+KiDS	440	8	$\sigma_s = \infty$	67.3	6.7 $\sigma$	513.9	8.4	2.9 $\sigma$
			$\sigma_s = 0.3$	59.9	6.2 $\sigma$	519.5	4.1	2.9 $\sigma$
DES+ACT	330	11	$\sigma_s = \infty$	37.5	3.9 $\sigma$	363.8	9.2	2.0 $\sigma$
			$\sigma_s = 0.3$	17.8	1.7 $\sigma$	371.6	5.0	2.1 $\sigma$
HSC+KiDS	180	8	$\sigma_s = \infty$	53.3	5.7 $\sigma$	222.4	6.2	2.7 $\sigma$
			$\sigma_s = 0.3$	62.4	6.4 $\sigma$	222.7	3.3	2.5 $\sigma$
HSC+ACT	70	11	$\sigma_s = \infty$	21.0	2.1 $\sigma$	66.0	9.3	1.0 $\sigma$
			$\sigma_s = 0.3$	16.9	1.6 $\sigma$	68.1	4.8	0.9 $\sigma$
KiDS+ACT	130	11	$\sigma_s = \infty$	43.5	4.4 $\sigma$	166.1	8.6	2.8 $\sigma$
			$\sigma_s = 0.3$	38.3	4.0 $\sigma$	171.5	4.3	2.9 $\sigma$
DES+HSC+KiDS	500	8	$\sigma_s = \infty$	69.8	6.9 $\sigma$	581.7	8.7	3.0 $\sigma$
			$\sigma_s = 0.3$	71.8	7.0 $\sigma$	586.7	4.5	3.0 $\sigma$
DES+HSC+ACT	390	11	$\sigma_s = \infty$	38.5	4.0 $\sigma$	435.5	9.8	2.2 $\sigma$
			$\sigma_s = 0.3$	29.2	3.1 $\sigma$	441.8	5.3	2.3 $\sigma$
DES+KiDS+ACT	450	11	$\sigma_s = \infty$	64.8	6.1 $\sigma$	534.1	9.8	3.2 $\sigma$
			$\sigma_s = 0.3$	49.0	4.9 $\sigma$	542.6	5.1	3.3 $\sigma$
HSC+KiDS+ACT	190	12	$\sigma_s = \infty$	59.7	5.6 $\sigma$	231.4	9.6	2.7 $\sigma$
			$\sigma_s = 0.3$	59.3	5.5 $\sigma$	234.5	5.1	2.7 $\sigma$
DES+HSC+KiDS+ACT	510	11	$\sigma_s = \infty$	65.4	6.1 $\sigma$	603.2	10.1	3.3 $\sigma$
			$\sigma_s = 0.3$	60.2	5.8 $\sigma$	610.2	5.6	3.3 $\sigma$

tension reported for COSEBIs in [Asgari et al. \(2021\)](#). Again, we refer the reader to more recent results from the KiDS-Legacy dataset ([Wright et al. 2025](#)).

### 5.2. Combining data sets

There are two important caveats to combining lensing surveys and providing joint constraints on deviations from the *Planck*  $\Lambda$ CDM matter power spectrum.

Firstly, as with combining any two data sets, we check that the data sets are not in tension. We employ *Tensiometer* ([Raveri et al. 2020](#); [Raveri and Doux 2021](#)) to test whether the unsmoothed  $\alpha(k)$  posteriors are reasonably consistent across the  $k$ -range, such that any smoothing prior is not double counted. In particular, we compute the non-Gaussian parameter-shift metric  $\Delta_{\text{NG}}$  introduced in [Raveri and Doux \(2021\)](#), which uses normalizing flows to model the parameter-difference distributions (see Section 7 for an illustration, comparing ACT vs. DES+HSC). We report their significance  $n_\sigma$  in units of Gaussian standard deviations, given this time by  $n_\sigma = \sqrt{2} \text{erf}^{-1}(\Delta_{\text{NG}})$ , in Table 4.<sup>8</sup> We find that

all dataset combinations show reasonable consistency (tensions below  $\sim 2 \sigma$ ) when considering the full-dimensional unsmoothed  $\alpha(k)$  posteriors. As expected from a visual inspection of Fig. 5, the galaxy-lensing surveys can be readily combined. Figure 6 shows an example comparison of constraints from DES and KiDS, along with their combined constraint.

A second important consideration, illustrated in Fig. 1, is the limited overlap in scale and redshift between CMB-lensing and galaxy-lensing surveys. Even the effective redshift for  $\alpha(k)$  constraints differs slightly between HSC and KiDS/DES. Therefore, these surveys may probe different physics, and we advise caution when interpreting our results. Combining these datasets can yield meaningful constraints for new physics that causes either a truly redshift-independent shift in the matter power spectrum, or redshift-independent deviations within the surveys' redshift range (even if redshift-dependent outside of it). However, joint analyses should be avoided if the new

<sup>8</sup> We also computed the Gaussian parameter-shift metric  $Q_{\text{UDM}}$  in update form as defined in [Raveri et al. \(2020\)](#). However, even though *Tensiometer* selects the bins where the posterior is at least 10% tighter than the prior, where most of the signal is confined and where posteriors are more Gaussian, we found it remained unstable for such non-Gaussian posterior distributions.

<sup>8</sup> We also computed the Gaussian parameter-shift metric  $Q_{\text{UDM}}$  in update

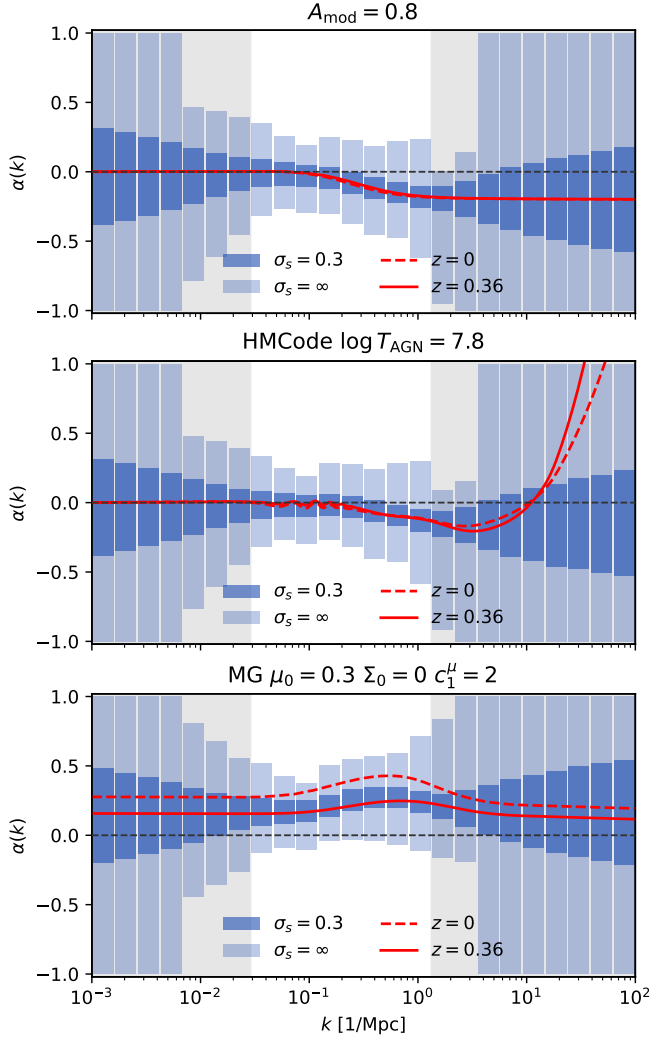


FIG. 4.— Validation tests performed using mock data generated at *Planck*  $\Lambda$ CDM cosmological parameters, incorporating various deviations to the standard nonlinear power spectrum. For each panel, the posterior of each component of  $\alpha = (\alpha(k_1), \dots, \alpha(k_{n_k}))$  is visualized as a box. The vertical extent of the boxes represents the 68% limits of the posterior, computed with `GetDist` (Lewis 2019). The horizontal extent corresponds to the width of the logarithmic  $k$ -bins. Dark blue boxes represent the posterior with smoothing ( $\sigma_s = 0.3$ ), while light blue boxes show the posterior without smoothing ( $\sigma_s = \infty$ ). The red lines indicate the relative differences between the injected and fiducial power spectra, evaluated at  $z = 0$  and at the effective DES redshift  $z_{\text{eff}} = 0.36$ . Note that any divergence between the posterior and smoothed posterior boxes in regions of low data sensitivity does not necessarily invalidate the recovery of the input cosmology. In the gray regions, the posterior distribution is dominated by the prior, and it is either uniform (no smoothing) or favors flat curves that satisfy the smoothing prior. *Top panel*: a deviation following the  $A_{\text{mod}}$  parametrization of Amon and Efstathiou (2022) is successfully recovered. *Middle panel*: baryonic feedback was modelled using `HMCode` (Mead et al. 2021) and the injected deviations were recovered within the constrained  $k$ -range, denoted by the unshaded band between gray regions. *Bottom panel*: a  $(\Sigma, \mu)$  modified-gravity model was implemented. While the deviation at the effective DES redshift ( $z_{\text{eff}} = 0.36$ ) was recovered, the redshift-dependent deviation from the  $\Lambda$ CDM power spectrum was not captured by our only-scale-dependent model, as expected.

physics introduces redshift-dependent modifications within the probed redshift range, as this would affect the different experiments unequally.

Table 3 presents the  $\alpha(k)$  tensions and goodness-of-fits for all dataset combinations. Our simple linear model provides a reasonable fit ( $n_\sigma \lesssim 2.5\sigma$ ) in all cases not involving KiDS, with or without smoothing, and the fit quality degrades slightly

TABLE 4

This table summarizes the consistency between all data subsets used in this analysis, based on the unsmoothed  $\alpha(k)$  posteriors. Consistency is quantified using the non-Gaussian parameter-shift metric  $\Delta_{\text{NG}}$  computed with `Tensimeter` on the full-dimensional, unsmoothed  $\alpha(k)$  posteriors.

Data subsets ( $\sigma_s = \infty$ )	$\Delta_{\text{NG}}$
DES vs. HSC	0.02 $\sigma$
DES vs. KiDS	0.02 $\sigma$
DES vs. ACT	0.14 $\sigma$
HSC vs. KiDS	< 0.01 $\sigma$
HSC vs. ACT	< 0.01 $\sigma$
KiDS vs. ACT	< 0.01 $\sigma$
DES vs. HSC+KiDS	0.26 $\sigma$
DES vs. HSC+ACT	1.06 $\sigma$
DES vs. KiDS+ACT	0.89 $\sigma$
HSC vs. DES+KiDS	0.01 $\sigma$
HSC vs. DES+ACT	0.14 $\sigma$
HSC vs. KiDS+ACT	< 0.01 $\sigma$
KiDS vs. DES+HSC	0.01 $\sigma$
KiDS vs. DES+ACT	0.31 $\sigma$
KiDS vs. HSC+ACT	< 0.01 $\sigma$
ACT vs. DES+HSC	0.42 $\sigma$
ACT vs. DES+KiDS	0.52 $\sigma$
ACT vs. HSC+KiDS	< 0.01 $\sigma$
DES vs. HSC+KiDS+ACT	1.50 $\sigma$
HSC vs. DES+KiDS+ACT	0.02 $\sigma$
KiDS vs. DES+HSC+ACT	0.13 $\sigma$
ACT vs. DES+HSC+KiDS	0.69 $\sigma$
DES+HSC vs. KiDS+ACT	0.72 $\sigma$
DES+KiDS vs. HSC+ACT	1.03 $\sigma$
DES+ACT vs. HSC+KiDS	0.63 $\sigma$

with the addition of more data. Figure 6 compares constraints obtained individually from DES and KiDS and their combination, which were jointly analyzed in *Dark Energy Survey and Kilo-Degree Survey Collaboration et al. (2023)*. Figure 7 compares constraints from the combined DES and HSC galaxy surveys with those from ACT, and their joint constraints. The galaxy surveys prefer a 20% lower projected power spectrum than the fiducial, dark-matter-only power spectrum. The ACT data, consistent with the fiducial model, pulls  $\alpha(k)$  towards zero in the range  $k \sim 0.01 \text{ Mpc}^{-1} - 0.1 \text{ Mpc}^{-1}$ , thus reducing the tension from  $4.4\sigma$  to  $3.1\sigma$ , at the price of a slightly worse fit. We also show the theoretical prediction obtained with `HMCode` to account for the effects of baryonic feedback, and find that the tension diminishes to  $0.8\sigma$  for DES+HSC+ACT ( $2.4\sigma$  for DES+HSC) with a baryonic feedback parameter of  $\log T_{\text{AGN}} = 8.4$ . Although we state once again that these constraints should be interpreted with caution, the combination of these data is able to constrain two orders of magnitudes of physical scales, from  $0.01 \text{ Mpc}^{-1}$  to  $1 \text{ Mpc}^{-1}$ .

## 6. APPLICATIONS

In the previous sections, we reconstructed scale-dependent deviations  $\alpha(k)$  to the *Planck*  $\Lambda$ CDM matter power spectrum, at the effective redshifts probed by galaxy- and CMB-lensing observations. We now describe how these results can be used to constrain extensions of the  $\Lambda$ CDM model that modify matter density perturbations. This section outlines a general methodology for such an analysis, highlights important caveats, and demonstrates its application to specific physical models.

### 6.1. Constraining power spectrum models

The core idea is to use the posterior distributions of  $\alpha(k)$  as a derived likelihood function to test alternative models of structure formation—analogue to how BAO analyses first extract the BAO scale along and across the line of sight before

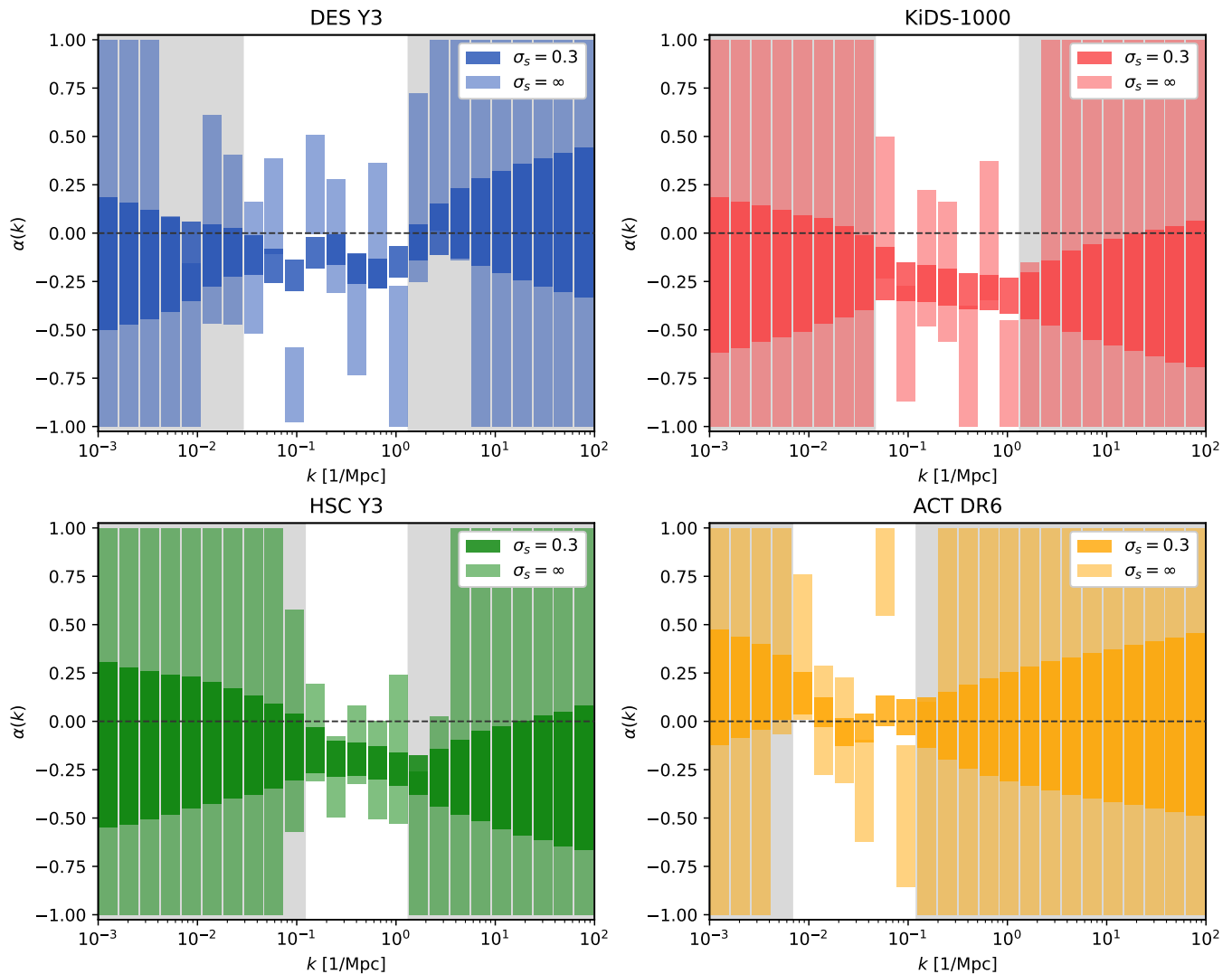


FIG. 5.— Constraints from individual lensing surveys on  $\alpha(k)$  defined as  $P(k, z) \equiv (1 + \alpha(k))P_{\text{fid}}(k, z)$  where  $P_{\text{fid}}(k, z)$  is the nonlinear  $\Lambda$ CDM matter power spectrum at *Planck* cosmology (see Table 2) computed with *halofit*. Table 1 shows the effective scales and redshifts probed by these experiments. Boxes are used to represent the 68% credible intervals derived from the posterior distributions of  $\alpha(k)$  computed in 24 logarithmically-spaced  $k$ -bins. Lighter shaded boxes represent the unsmoothed, more strongly anti-correlated  $k$ -bins, while darker boxes show the smoothed, decorrelated bins (smoothing scale  $\sigma_s = 0.3$ ). The gray shaded regions indicate where each dataset loses sensitivity, and where the points become strongly correlated (see Figs. 2 and 3). We note that our model does not include intrinsic alignments and baryonic feedback, which could contribute to the lower power spectrum observed by cosmic shear surveys. Results adopting a DES Y3 cosmology (Doux *et al.* 2022) as fiducial are shown in Section 7.

fitting cosmological models to those measurements (Adame *et al.* 2025). We construct this likelihood directly from the  $\alpha(k)$  posteriors and recommend restricting comparisons to the  $k$ -range where the data meaningfully constrain  $\alpha(k)$ . Our results show that, when a smoothing prior of width  $\sigma_s = 0.3$  is applied, the  $\alpha(k)$  posteriors are well approximated by a multivariate Gaussian within the constrained  $k$ -range. For unsmoothed posteriors, a truncated multivariate Gaussian may be more appropriate.

This likelihood can then be used to test the predictions of extended cosmological models. Compared to traditional approaches that reduce lensing data to a single summary statistic like  $S_8$ , this method preserves the full scale-dependent information available in the data. Since  $\alpha(k)$  is defined at the effective redshift of the lensing data, comparisons must be made at the corresponding redshifts. For combined datasets with differing redshift sensitivities, a first approximation is to treat the  $\alpha(k)$  constraints from each experiment as independent likelihoods, thereby constraining the model at multiple

redshifts.

### 6.1.1. Caveats

While this methodology is powerful, it is subject to several caveats. The reconstruction of  $\alpha(k)$  relies on a fiducial cosmology, and thus a specific projection from the angular power spectra  $C_\ell$  into  $P(k, z)$ , as per Eq. (5). This projection enables intuitive comparison between inferred deviations and theoretical models but assumes that the *background* cosmology is fixed. If an extended model also alters the background expansion (e.g., changes in  $\Omega_m, H_0$ ), the window functions used in the  $\alpha(k)$  inference in Eq. (6) will no longer be valid. The practical impact of switching the fiducial baseline is illustrated in Section 7. In addition, the relationship between physical scales  $k$  and angular scales  $\ell$  would also be altered. We illustrate this in Fig. 8 by varying background  $\Lambda$ CDM parameters<sup>9</sup>

<sup>9</sup> Note that here we follow the DES modeling of neutrinos as three massive species with degenerate mass.

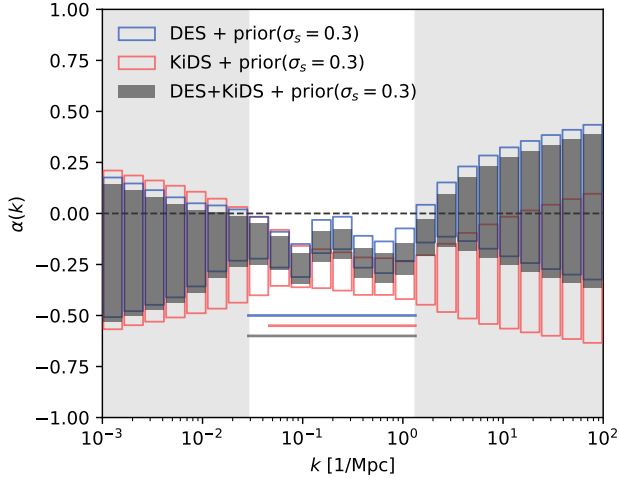


FIG. 6.— Constraints on  $\alpha(k)$  from DES Y3 (red), KiDS-1000 (blue), and their combination (gray boxes), using the standard  $\sigma_s = 0.3$  smoothing prior. Horizontal lines show the  $k$ -regions constrained by each of these data sets, while the unshaded region corresponds to constraints for DES+KiDS.

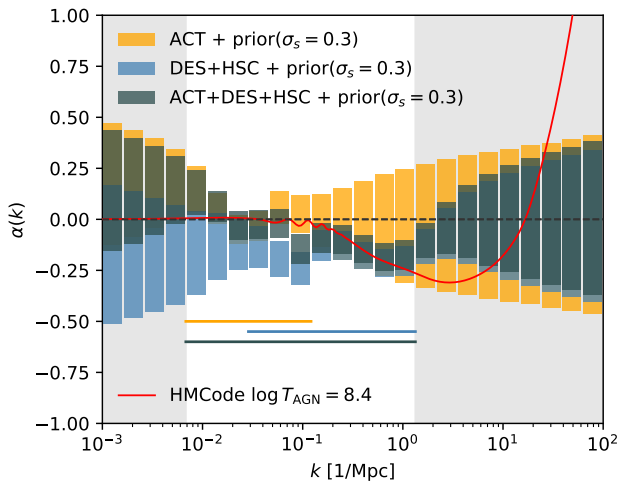


FIG. 7.— Constraints on  $\alpha(k)$  from ACT DR6 (yellow), DES Y3 combined with HSC Y3 (blue), and their combination (dark gray boxes), using the standard  $\sigma_s = 0.3$  smoothing prior. Horizontal lines show the  $k$ -regions constrained by each of these data sets, while the unshaded region corresponds to constraints for ACT+DES+KiDS. We overplot the theoretical prediction for baryonic feedback parameter  $\log T_{\text{AGN}} = 8.4$  computed using HMCode in red, showing good agreement throughout the constrained range. See Section 7 for a subset of the two-dimensional marginal distributions for these datasets.

and showing that the resulting constraints differ from those obtained directly from the lensing  $C_\ell$  spectra. Although it is in principle possible to repeat the full  $\alpha(k)$  inference at a different fiducial background, these caveats still remain, they are simply offset by a different fiducial cosmology.

Further limitations arise, for instance, in modified gravity models parameterized by  $\mu$  and  $\Sigma$ , where matter and light respond to different gravitational potentials. In such cases, the lensing-inferred  $\alpha(k)$  may not directly correspond to modifications in the matter power spectrum, breaking the assumption that a single  $P(k, z)$  governs both observables.

Finally, if the model does not induce an overall rescaling of the matter power spectrum, it may not fit both large and small scale  $\alpha(k)$  equally well. In such cases, we recommend

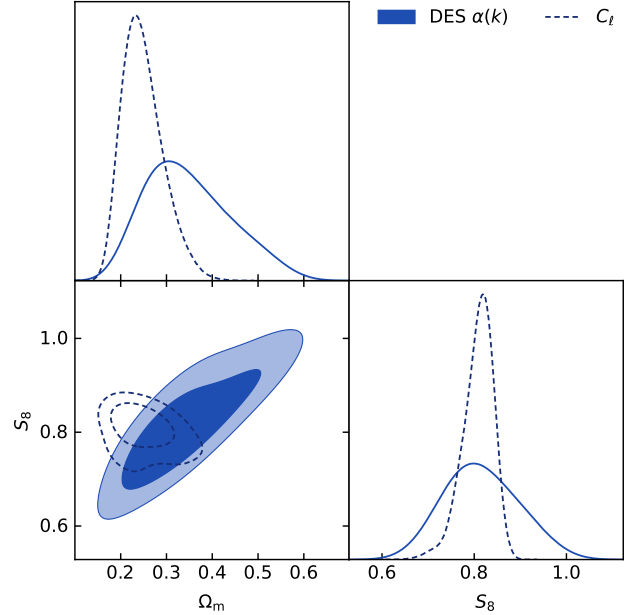


FIG. 8.— Constraints on the  $\Lambda$ CDM parameters  $\sigma_8$  and  $\Omega_m$  derived from the  $\alpha(k)$  likelihood function (solid, filled posteriors) are compared to those obtained using standard power spectrum analyses (dashed posteriors) for DES Y3 data (using a scale cut at  $k_{\text{max}} = 1 h \text{ Mpc}^{-1}$ , see section 3.5.2 of Doux *et al.* (2022)). While the mean parameter values are broadly consistent, we caution that varying background cosmological parameters is formally inconsistent with our inference framework, which assumes a fixed  $\Lambda$ CDM cosmology—particularly in the construction of the window functions (see Eq. (6)).

allowing the amplitude of scalar perturbations (e.g.,  $A_s$  or  $\sigma_8$ ) to vary in the model comparison. This ensures that any scale-dependent deviation provides a globally consistent fit to the reconstructed  $\alpha(k)$ . In general, one must verify that the extended model yields a good fit to the data-constrained  $\alpha(k)$ , with the result depending on which model parameters are allowed to vary.

### 6.1.2. Constraints

We demonstrate the utility of this approach by applying it to two physical scenarios. Model predictions are generated using the CCL cosmology library, with parameter inference performed via the Nautilus nested-sampling algorithm (Lange 2023).

First, we constrain a phenomenological amplitude modifier  $A_{\text{mod}}$  which suppresses power at small scales, while jointly varying  $\sigma_8$  to accommodate the large-scale amplitude. Our constraints from individual surveys are consistent with those obtained from direct  $C_\ell$  analyses at fixed background cosmology, as shown in Fig. 9. This agreement holds across smoothing priors and when restricting to only the well-constrained  $k$ -range. All three galaxy surveys prefer lower values of  $\sigma_8$ , with constraints that are anticorrelated with  $A_{\text{mod}}$ . In contrast, ACT does not tightly constrain  $A_{\text{mod}}$ , as it primarily probes the matter power spectrum at  $z \sim 2$  and on scales where nonlinear effects are subdominant. Reconciling the lower  $\sigma_8$  preferred by galaxy lensing within  $\Lambda$ CDM with the higher value inferred from ACT thus requires a suppression of small-scale power, corresponding to  $A_{\text{mod}} < 1$ .

Second, we apply our method to constrain baryonic feedback as modeled in HMCode, using the AGN heating parameter  $\log T_{\text{AGN}}$ . Individual experiments do not independently constrain both  $\sigma_8$  and  $\log T_{\text{AGN}}$ , but combining their  $\alpha(k)$  likelihoods allows for joint inference. We consider the com-

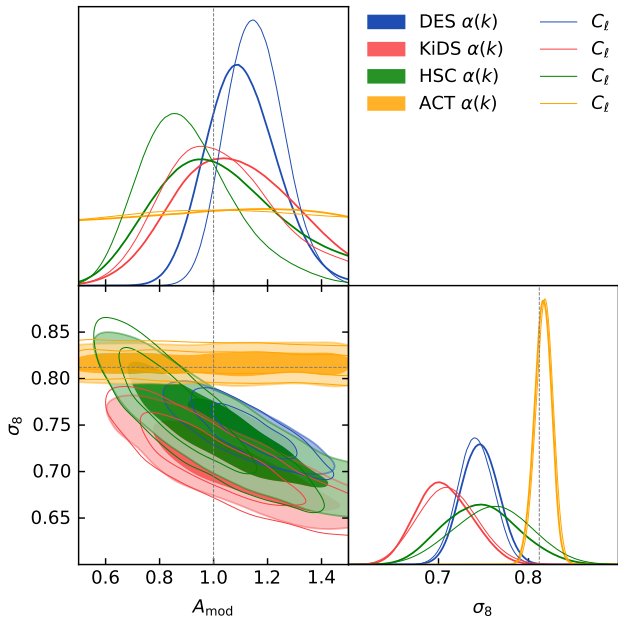


FIG. 9.— Constraints on the  $A_{\text{mod}}$  model derived from the  $\alpha(k)$ -based likelihood (filled contours), with  $\sigma_8$  varied and all other parameters fixed to their *Planck* values. For comparison, constraints obtained directly from the angular power spectra are shown as unfilled contours (and thin lines in one-dimensional marginal panels). Dashed lines indicate the fiducial value  $A_{\text{mod}} = 1$  and the *Planck* best-fit value of  $\sigma_8$ .

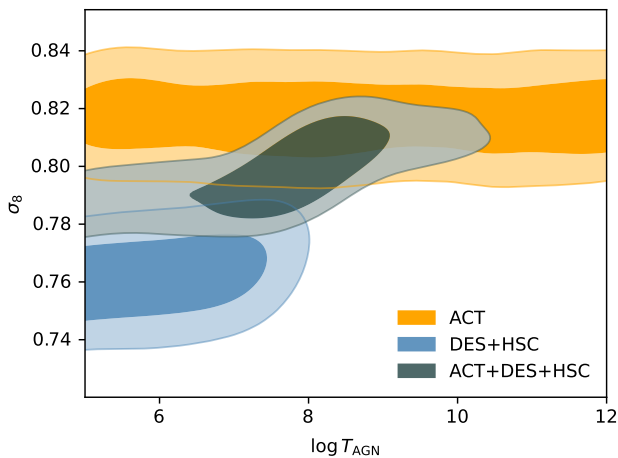


FIG. 10.— Constraints on baryonic feedback as modeled in HMCode, derived from the  $\alpha(k)$ -based likelihoods of ACT, DES, and HSC treated independently. Rather than using the joint constraints on  $\alpha(k)$  shown in Fig. 7, this result combines the single-experiment posteriors as independent likelihoods. bination of DES, HSC and ACT data, for which our model provided an acceptable fit (see Table 3). While DES and HSC favor a lower  $\sigma_8$  value seemingly inconsistent with ACT as shown in Fig. 10, their combined likelihoods constrain both parameters with a reasonable fit, and we obtain

$$\log T_{\text{AGN}} = 7.76^{+0.87}_{-0.69},$$

demonstrating the power of combining datasets with complementary redshift and scale sensitivities.

### 6.2. Plug-and-play implementations

To facilitate reproducibility and encourage further exploration, we provide a comprehensive GitHub repository accompanying this work. The repository includes all the data and

code used in our analysis, along with intermediate products such as the computed window functions and the covariances marginalized over observational systematics. It also contains posterior samples for  $\alpha(k)$  and a Jupyter notebook that walks through the complete analysis workflow.

The demonstration notebook is designed to guide users through each stage of the pipeline, allowing them to reproduce the main results of our study with minimal setup. Specifically, it covers:

- Loading and pre-processing the weak-lensing data, with results saved for direct reuse.
- Extracting the deviations  $\alpha(k)$  from the matter power spectrum  $P(k, z)$  using efficient Hamiltonian Monte Carlo (HMC) inference.
- Comparing the inferred  $\alpha(k)$  with predictions from the  $\Lambda$ CDM model.
- Exploring extensions to the  $\Lambda$ CDM model’s predictions, as discussed in the previous section.

These files enable the user to reproduce our entire analysis at the fiducial cosmology of their choosing, potentially mitigating one of the principal caveats of this approach. By shifting the fiducial cosmology to the best-fit parameters of an extended model inferred from external data (*e.g.* CMB data), or to theoretically motivated values, the resulting  $\alpha(k)$  posteriors will reflect deviations relative to a new baseline. The user can then draw conclusions based on the level of tension between the updated  $\alpha(k)$  posteriors and the new zero-point defined by their chosen model. Note that this approach remains tied to the choice of a single fiducial cosmology.

In addition, we provide a set of pre-constructed  $\alpha(k)$  likelihood modules compatible with the widely-used cosmological inference code *MontePython* (Audren *et al.* 2013; Brinckmann and Lesgourgues 2019). Each module includes the necessary components to define a multivariate Gaussian likelihood over the constrained  $k$  range: the  $k$  vector, the mean  $\alpha(k)$  vector, the inverse covariance matrix, the effective redshift of the measurement, and the fiducial power spectrum at that redshift for those  $k$ . We also include a notebook that extracts these components from the  $\alpha(k)$  posteriors computed above, and an example input file for using this likelihood with *MontePython*. Our provided framework is compatible with modifying the fiducial cosmology and producing alternate  $\alpha(k)$  likelihoods. This setup allows for straightforward integration of our results into broader cosmological parameter-estimation efforts.

## 7. CONCLUSIONS

In this work, we introduced a framework for directly inferring scale-dependent deviations from the matter power spectrum  $P(k, z)$  using galaxy- and CMB-lensing surveys. By extracting this information beyond the traditional  $S_8$  summary statistic, our method identifies where current observations may deviate from *Planck*  $\Lambda$ CDM predictions as a function of scale at the effective redshift of each survey. This enables a more detailed and flexible characterization of structure growth, capturing deviations that could otherwise be overlooked. The approach is fast, adaptable, and fully reproducible, and we have released an accompanying GitHub repository to support further exploration and integration into cosmological inference pipelines.

Specifically, we inferred  $\alpha(k) \equiv P(k)/P_{\text{fid}}(k) - 1$  over 24 logarithmic  $k$ -bins in the range  $10^{-3} \text{ Mpc}^{-1}$  to  $10^2 \text{ Mpc}^{-1}$  using HMC sampling with a data-driven smoothing prior, and applied our method independently and jointly to lensing data from DES Y3, KiDS-1000, HSC Y3, and ACT DR6. In practice, this allows us to recover the *projected* power spectrum probed by lensing surveys, which can include the combined effects of baryonic feedback and intrinsic alignments, without requiring explicit modeling of these processes. For galaxy lensing surveys, we used angular multipoles up to  $l_{\text{max}} \sim 2000$ , and all results assume fixed cosmology with analytic marginalization over shear calibration and redshift distribution uncertainties. All deviations are reported with respect to the *Planck*  $\Lambda$ CDM prediction for a CDM-only (i.e., neglecting baryonic feedback and intrinsic alignments) matter power spectrum. Interpreting  $\alpha(k)$  as the scale-dependent deviation in the projected matter power spectrum probed by lensing, our key findings are:

- DES, KiDS, and HSC all show a 15–30% suppression of power at  $k \sim 0.1 \text{ Mpc}^{-1} - 1 \text{ Mpc}^{-1}$  relative to *Planck*, with combined tensions reaching  $4\sigma$  for DES+HSC at fixed cosmology (Fig. 5 and Table 3).
- ACT data are consistent with  $\Lambda$ CDM, indicating that the suppression is either redshift-dependent and specific to lower  $z$ , or restricted to small scales  $k \gtrsim 0.1 \text{ Mpc}^{-1}$ .
- Dataset tensions assessed using non-Gaussian metrics from *Tensiometer* are mild and generally within  $2\sigma$ , allowing for robust joint analyses (Table 4).
- The combined ACT, DES and HSC datasets constrain  $\alpha(k)$  over  $k \sim 0.01 \text{ Mpc}^{-1} - 1 \text{ Mpc}^{-1}$ , extending across two decades in scale, consistent with *Planck* at  $k \lesssim 0.1 \text{ Mpc}^{-1}$  and 10–25% lower at smaller scales (Figs. 7, C1 and C2).
- Our results, which are agnostic to the physical origin of deviations, are both qualitatively and quantitatively consistent with previous studies.

We also demonstrated the utility of the derived  $\alpha(k)$  likelihoods by constraining physical models such as baryonic feedback and a phenomenological suppression of power (Figs. 9 and 10), recovering results consistent with direct  $C_\ell$  analyses and enabling joint constraints across datasets with complementary scale and redshift sensitivity. To simplify reproducibility and implementation of our entire analysis, we provide a GitHub repository with code, data, results, and  $\alpha(k)$  likelihoods compatible with *MontePython* which enable fast comparison with theoretical models. As the  $\alpha(k)$  are constrained at a specific fiducial cosmology, switching this to a different theoretical cosmology will shift  $\alpha(k)$  constraints, as

illustrated in Section 7 using a DES Y3 cosmology. These new constraints can then help the user determine if the new cosmology can explain lensing power spectra or if deviations are still preferred, effectively capturing how well lensing data are fit by the new model.

Looking ahead, two key developments could substantially expand the reach and robustness of this framework. First, while our current method constrains deviations as a function of scale alone, future extensions could allow for joint inference of  $\alpha(k, z)$  over both scale and redshift. This would capture the temporal evolution of structure growth, potentially disentangling physical effects (e.g., modified gravity or time-varying dark energy) from observational systematics that evolve differently with redshift. It would also allow for a more complete comparison across datasets with different redshift sensitivities, such as galaxy and CMB lensing.

Second, the Limber projection from angular power spectra  $C_\ell$  to  $P(k, z)$  currently relies on a fiducial cosmology to relate redshifts to comoving distances. While this is reasonable for internal consistency, it implicitly assumes the background expansion history of  $\Lambda$ CDM. To increase model-independence, future versions of this analysis could replace this assumption with empirically determined distance-redshift relations, e.g., from Type Ia supernovae or BAO measurements. This would allow the lensing data to test the growth of structure with minimal reliance on background model assumptions, enhancing the interpretability of any detected deviations.

Together, these extensions would enable sharper identification of possible tensions with  $\Lambda$ CDM as a function of both scale and cosmic time. However, current data may not provide sufficient sensitivity to fully realize this potential. The next generation of surveys—including the Rubin Observatory Legacy Survey of Space and Time (LSST), ESA’s *Euclid* mission, and NASA’s *Roman* Space Telescope—will dramatically improve weak-lensing power-spectrum measurements by delivering deeper, wider, and higher-resolution data. Combined with our scalable and model-flexible framework, these advances will significantly tighten constraints on  $\alpha(k, z)$  and enhance our ability to probe the fundamental physics driving the growth of cosmic structure.

#### ACKNOWLEDGMENTS

We thank Marco Gatti, Wayne Hu, Bhuvnesh Jain, Meng-Xiang Lin, Mat Madhavacheril, Shivam Pandey, and Marco Raveri for stimulating and fruitful discussions. We are grateful to Roohi Dalal for providing the HSC cosmic shear data and thank Rafael C. H. Gomes for his input during the early stages of this analysis. TK was supported by the Kavli Institute for Cosmological Physics at the University of Chicago through an endowment from the Kavli Foundation. Computing resources were provided by the National Energy Research Scientific Computing Center (NERSC), and the University of Chicago Research Computing Center through the Kavli Institute for Cosmological Physics.

#### REFERENCES

- L. F. Secco, S. Samuroff, E. Krause, *et al.*, *Phys. Rev. D* **105**, 023515 (2022), [arXiv:2105.13544 \[astro-ph.CO\]](#).  
A. Amon, D. Gruen, M. A. Troxel, *et al.*, *Phys. Rev. D* **105**, 023514 (2022), [arXiv:2105.13543 \[astro-ph.CO\]](#).  
C. Doux, B. Jain, D. Zeurher, *et al.*, *MNRAS* **515**, 1942 (2022), [arXiv:2203.07128 \[astro-ph.CO\]](#).  
R. Dalal, X. Li, A. Nicola, *et al.*, *Phys. Rev. D* **108**, 123519 (2023), [arXiv:2304.00701 \[astro-ph.CO\]](#).  
M. Asgari, C.-A. Lin, B. Joachimi, *et al.*, *A&A* **645**, A104 (2021), [arXiv:2007.15633 \[astro-ph.CO\]](#).  
Dark Energy Survey and Kilo-Degree Survey Collaboration, T. M. C. Abbott, M. Aguena, *et al.*, *The Open Journal of Astrophysics* **6**, 36 (2023), [arXiv:2305.17173 \[astro-ph.CO\]](#).  
M. S. Madhavacheril, F. J. Qu, B. D. Sherwin, *et al.*, *ApJ* **962**, 113 (2024), [arXiv:2304.05203 \[astro-ph.CO\]](#).  
F. J. Qu, B. D. Sherwin, M. S. Madhavacheril, *et al.*, *ApJ* **962**, 112 (2024), [arXiv:2304.05202 \[astro-ph.CO\]](#).

- Planck Collaboration, N. Aghanim, Y. Akrami, *et al.*, *A&A* **641**, A6 (2020), arXiv:1807.06209 [astro-ph.CO].
- A. H. Wright, B. Stölzner, M. Asgari, *et al.*, arXiv e-prints , arXiv:2503.19441 (2025), arXiv:2503.19441 [astro-ph.CO].
- L. F. Secco, T. Karwal, W. Hu, and E. Krause, *Phys. Rev. D* **107**, 083532 (2023), arXiv:2209.12997 [astro-ph.CO].
- M. Tegmark and M. Zaldarriaga, *Phys. Rev. D* **66**, 103508 (2002), arXiv:astro-ph/0207047 [astro-ph].
- J. Lesgourgues, arXiv e-prints , arXiv:1104.2932 (2011), arXiv:1104.2932 [astro-ph.IM].
- A. Lewis, A. Challinor, and A. Lasenby, *ApJ* **538**, 473 (2000), arXiv:astro-ph/9911177 [astro-ph].
- The Dark Energy Survey Collaboration, arXiv e-prints , astro-ph/0510346 (2005), arXiv:astro-ph/0510346 [astro-ph].
- J. T. A. de Jong, G. A. Verdoes Kleijn, K. H. Kuijken, and E. A. Valentijn, *Experimental Astronomy* **35**, 25 (2013), arXiv:1206.1254 [astro-ph.CO].
- H. Aihara, N. Arimoto, R. Armstrong, *et al.*, *PASJ* **70**, S4 (2018), arXiv:1704.05858 [astro-ph.IM].
- D. S. Swetz, P. A. R. Ade, M. Amiri, *et al.*, *ApJS* **194**, 41 (2011), arXiv:1007.0290 [astro-ph.IM].
- A. Amon and G. Efstathiou, *MNRAS* **516**, 5355 (2022), arXiv:2206.11794 [astro-ph.CO].
- C. Preston, A. Amon, and G. Efstathiou, *MNRAS* **525**, 5554 (2023), arXiv:2305.09827 [astro-ph.CO].
- J. C. Broxterman and K. Kuijken, *A&A* **692**, A201 (2024), arXiv:2409.13404 [astro-ph.CO].
- T. M. C. Abbott, M. Aguena, A. Alarcon, *et al.*, *Phys. Rev. D* **107**, 083504 (2023), arXiv:2207.05766 [astro-ph.CO].
- M.-X. Lin, B. Jain, M. Raveri, *et al.*, *Phys. Rev. D* **109**, 063523 (2024), arXiv:2308.16183 [astro-ph.CO].
- R. Terasawa, X. Li, M. Takada, *et al.*, *Phys. Rev. D* **111**, 063509 (2025), arXiv:2403.20323 [astro-ph.CO].
- C. Preston, K. K. Rogers, A. Amon, and G. Efstathiou, arXiv e-prints , arXiv:2505.02233 (2025), arXiv:2505.02233 [astro-ph.CO].
- Z. Zhou and N. Weiner, arXiv e-prints , arXiv:2409.06771 (2024), arXiv:2409.06771 [hep-ph].
- J. Khoury, M.-X. Lin, and M. Trodden, arXiv e-prints , arXiv:2503.16415 (2025), arXiv:2503.16415 [astro-ph.CO].
- V. Poulin, J. L. Bernal, E. D. Kovetz, and M. Kamionkowski, *Phys. Rev. D* **107**, 123538 (2023), arXiv:2209.06217 [astro-ph.CO].
- M. Asghari, J. Beltrán Jiménez, S. Khosravi, and D. F. Mota, *JCAP* **04**, 042, arXiv:1902.05532 [astro-ph.CO].
- J. Beltrán Jiménez, D. Bettoni, D. Figueruelo, *et al.*, *Phys. Rev. D* **104**, 103503 (2021), arXiv:2106.11222 [astro-ph.CO].
- G. Ye, J.-Q. Jiang, and A. Silvestri, arXiv e-prints , arXiv:2411.07082 (2024), arXiv:2411.07082 [astro-ph.CO].
- C. Preston, A. Amon, and G. Efstathiou, *MNRAS* **533**, 621 (2024), arXiv:2404.18240 [astro-ph.CO].
- P. Simon, L. Porth, P. Burger, and K. Kuijken, arXiv e-prints , arXiv:2502.04449 (2025), arXiv:2502.04449 [astro-ph.CO].
- K. Perez Sarmiento, A. Laguë, M. Madhavacheril, *et al.*, arXiv e-prints , arXiv:2502.06687 (2025), arXiv:2502.06687 [astro-ph.CO].
- B. Audren, J. Lesgourgues, K. Benabed, and S. Prunet, *J. Cosmology Astropart. Phys.* **2013**, 001 (2013), arXiv:1210.7183 [astro-ph.CO].
- M. LoVerde and N. Afshordi, *Phys. Rev. D* **78**, 123506 (2008), arXiv:0809.5112 [astro-ph].
- R. Mandelbaum, *ARA&A* **56**, 393 (2018), arXiv:1710.03235 [astro-ph.CO].
- R. Takahashi, M. Sato, T. Nishimichi, *et al.*, *ApJ* **761**, 152 (2012), arXiv:1208.2701 [astro-ph.CO].
- D. Alonso, J. Sanchez, A. Slosar, and LSST Dark Energy Science Collaboration, *MNRAS* **484**, 4127 (2019), arXiv:1809.09603 [astro-ph.CO].
- A. Nicola, C. García-García, D. Alonso, *et al.*, *J. Cosmology Astropart. Phys.* **2021**, 067 (2021), arXiv:2010.09717 [astro-ph.CO].
- O. Abril-Pla, V. Andreani, C. Carroll, *et al.*, *PeerJ Computer Science* **9**, e1516 (2023).
- H. Hildebrandt, J. L. van den Busch, A. H. Wright, *et al.*, *A&A* **647**, A124 (2021), arXiv:2007.15635 [astro-ph.CO].
- B. Joachimi, C. A. Lin, M. Asgari, *et al.*, *A&A* **646**, A129 (2021), arXiv:2007.01844 [astro-ph.CO].
- S. L. Bridle, R. Crittenden, A. Melchiorri, *et al.*, *MNRAS* **335**, 1193 (2002), arXiv:astro-ph/0112114 [astro-ph].
- A. N. Taylor and T. D. Kitching, *MNRAS* **408**, 865 (2010), arXiv:1003.1136 [astro-ph.CO].
- C. García-García, D. Alonso, and E. Bellini, *J. Cosmology Astropart. Phys.* **2019**, 043 (2019), arXiv:1906.11765 [astro-ph.CO].
- O. Friedrich, F. Andrade-Oliveira, H. Camacho, *et al.*, *MNRAS* **508**, 3125 (2021), arXiv:2012.08568 [astro-ph.CO].
- N. E. Chisari, D. Alonso, E. Krause, *et al.*, *ApJS* **242**, 2 (2019), arXiv:1812.05995 [astro-ph.CO].
- M. Raveri, *Phys. Rev. D* **101**, 083524 (2020), arXiv:1902.01366 [astro-ph.CO].
- M. Raveri, G. Zacharegkas, and W. Hu, *Phys. Rev. D* **101**, 103527 (2020), arXiv:1912.04880 [astro-ph.CO].
- A. J. Mead, S. Brieden, T. Tröster, and C. Heymans, *MNRAS* **502**, 1401 (2021), arXiv:2009.01858 [astro-ph.CO].
- A. Lewis, arXiv e-prints , arXiv:1910.13970 (2019), arXiv:1910.13970 [astro-ph.IM].
- C. M. Hirata and U. Seljak, *Phys. Rev. D* **70**, 063526 (2004), arXiv:astro-ph/0406275 [astro-ph].
- S. Bridle and L. King, *New Journal of Physics* **9**, 444 (2007), arXiv:0705.0166 [astro-ph].
- M. Raveri and C. Doux, *Phys. Rev. D* **104**, 043504 (2021), arXiv:2105.03324 [astro-ph.CO].
- A. G. Adame, J. Aguilar, S. Ahlen, *et al.*, *J. Cosmology Astropart. Phys.* **2025**, 021 (2025), arXiv:2404.03002 [astro-ph.CO].
- J. U. Lange, *MNRAS* **525**, 3181 (2023), arXiv:2306.16923 [astro-ph.IM].
- T. Brinckmann and J. Lesgourgues, *Physics of the Dark Universe* **24**, 100260 (2019), arXiv:1804.07261 [astro-ph.CO].

## APPENDIX

### A. IMPACT OF SYSTEMATICS AND SCALE CUTS

Figure A1 shows  $\alpha(k)$  constraints for the four surveys varying some of the assumptions in our methodology as well as scale cuts, demonstrating the overall robustness of our results.

### B. IMPACT OF FIDUCIAL COSMOLOGY

To examine the dependence of our results on the choice of fiducial cosmology, we repeat the analysis of Section 5.1 using an alternative nonlinear matter power spectrum and corresponding window matrices computed at the mean cosmology inferred from the DES Y3 harmonic-space analysis (Doux *et al.* 2022), rather than from the *Planck* 2018  $\Lambda$ CDM cosmology (Planck Collaboration *et al.* 2020). Figure B1 compares the resulting  $\alpha(k)$  constraints for the four lensing surveys considered in this work under both cosmologies.

For the galaxy-lensing surveys, adopting the DES Y3 cosmology increases the overall amplitude of  $\alpha(k)$  relative to the

*Planck*-based results. DES becomes consistent with  $\alpha(k) = 0$ , as expected since the DES fiducial cosmology corresponds to the posterior mean of its own data. For HSC and KiDS,  $\alpha(k)$  remain lower than zero. This is consistent with the smaller level of tension between DES Y3 and *Planck* (see Fig. 16 of Doux *et al.* 2022) relative to *Planck* and HSC, KiDS, which still requires a suppression in  $\alpha(k)$ , albeit smaller, at this new fiducial. Beyond this overall amplitude shift, we find that the scale-dependence of  $\alpha(k)$  within the constrained  $k$ -range remains very similar between the two fiducial cosmologies, with a more pronounced discrepancy at intermediate scales ( $k \sim 0.1 \text{ Mpc}^{-1}$ ) than at nonlinear scales ( $k \sim 1 \text{ Mpc}^{-1}$ ), where differences between cosmologies become less significant. For ACT lensing, differences are even smaller and indistinguishable for  $k \gtrsim 0.03 \text{ Mpc}^{-1}$ .

### C. FULL POSTERiors FROM ACT, DES AND HSC

Figure C1 shows the one- and two-dimensional marginal distributions for constraints obtained from ACT, DES, HSC and their combinations. Figure C2 shows the parameter-difference

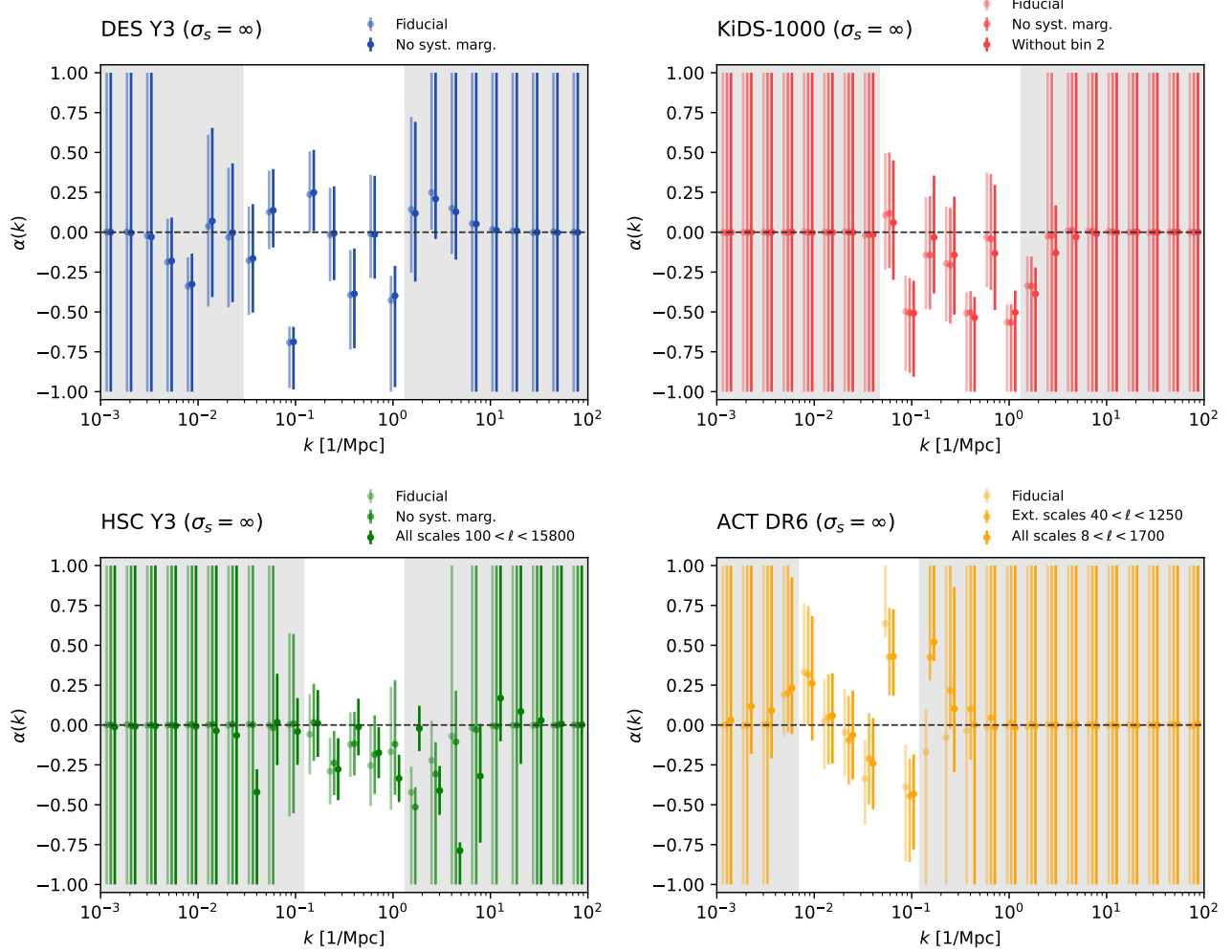


FIG. A1.— Constraints on  $\alpha(k)$  obtained from the four lensing surveys considered in this work, varying several assumptions. The fiducial case is that presented in Fig. 5, using analytic systematics marginalization and fiducial scale cuts. We present results obtained when ignoring this marginalization for galaxy surveys. We also explore several extended scale cuts for HSC and ACT, and the effect of removing the second redshift bin for KiDS. No smoothing prior is applied, such that data-driven variations may be appreciated.

distribution used in estimating the level of agreement between ACT and DES+HSC data before combining them.

#### D. COMPARING $\Lambda$ CDM CONSTRAINTS FROM $C_\ell$ AND $\alpha(k)$

Figure D1 compares the posteriors of subsets of  $\Lambda$ CDM parameters when constrained with the  $\alpha(k)$  likelihoods relative to those obtained from a full analysis of the shear power spectra  $C_\ell$  for DES Y3 data. We isolate an overall amplitude shift in  $\alpha(k)$  by fixing the amplitude  $A_s$  of the primordial power spectrum to *Planck*. We also separately fix the background

cosmology to the fiducial *Planck* cosmology by fixing  $\Omega_m$  and  $h$ . Lastly, we vary all  $\Lambda$ CDM parameters. None of these scenarios reproduces the same contour extents or degeneracy directions as the  $C_\ell$  posteriors, demonstrating that the two approaches have fundamentally different information contents.

This paper was built using the Open Journal of Astrophysics  $\LaTeX$  template. The OJA is a journal which provides fast and easy peer review for new papers in the `astro-ph` section of the arXiv, making the reviewing process simpler for authors and referees alike. Learn more at <http://astro.theoj.org>.

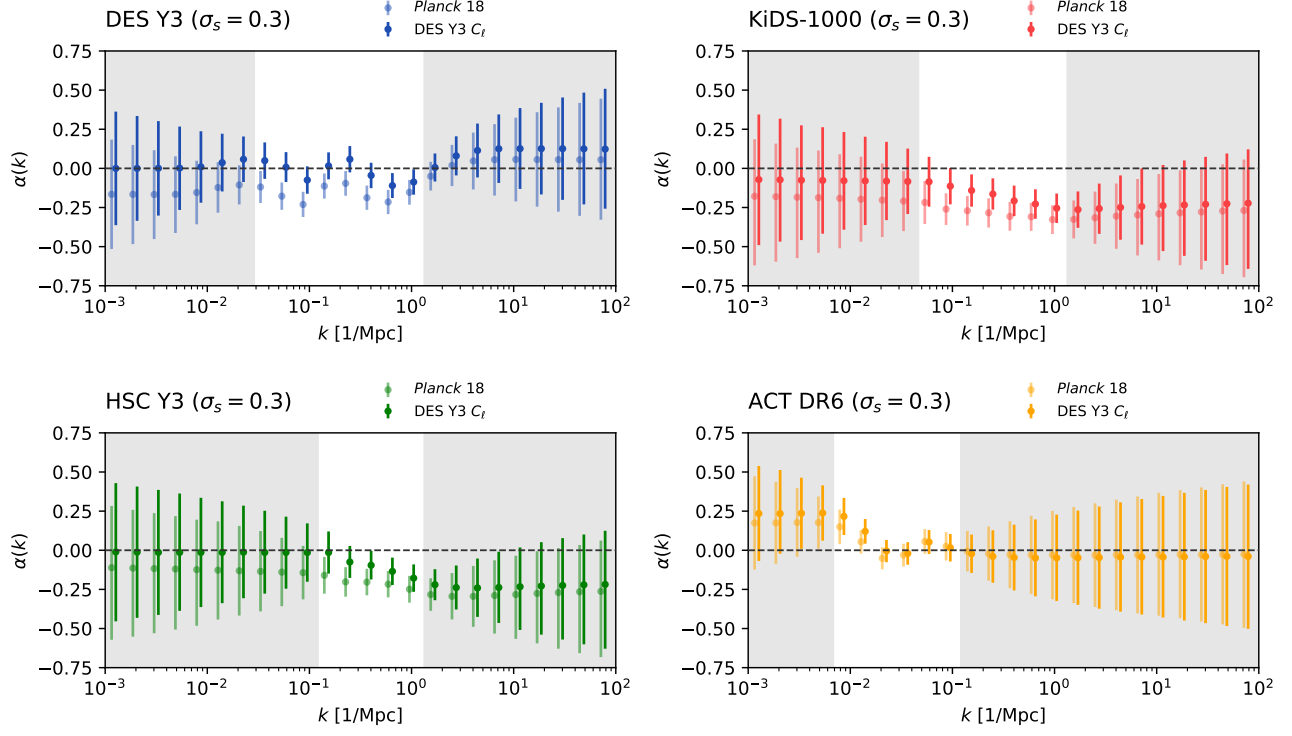


FIG. B1.— Constraints on  $\alpha(k)$  obtained from the four lensing surveys considered in this work, for two different fiducial cosmologies: *Planck* 2018  $\Lambda$ CDM (Planck Collaboration *et al.* 2020,  $\Omega_m = 0.316$ ,  $S_8 = 0.834$ , as shown in Fig. 5) and DES Y3 harmonic-space cosmic shear (Doux *et al.* 2022,  $\Omega_m = 0.257$ ,  $S_8 = 0.803$ ). A smoothing prior of  $\sigma_s = 0.3$  is applied.

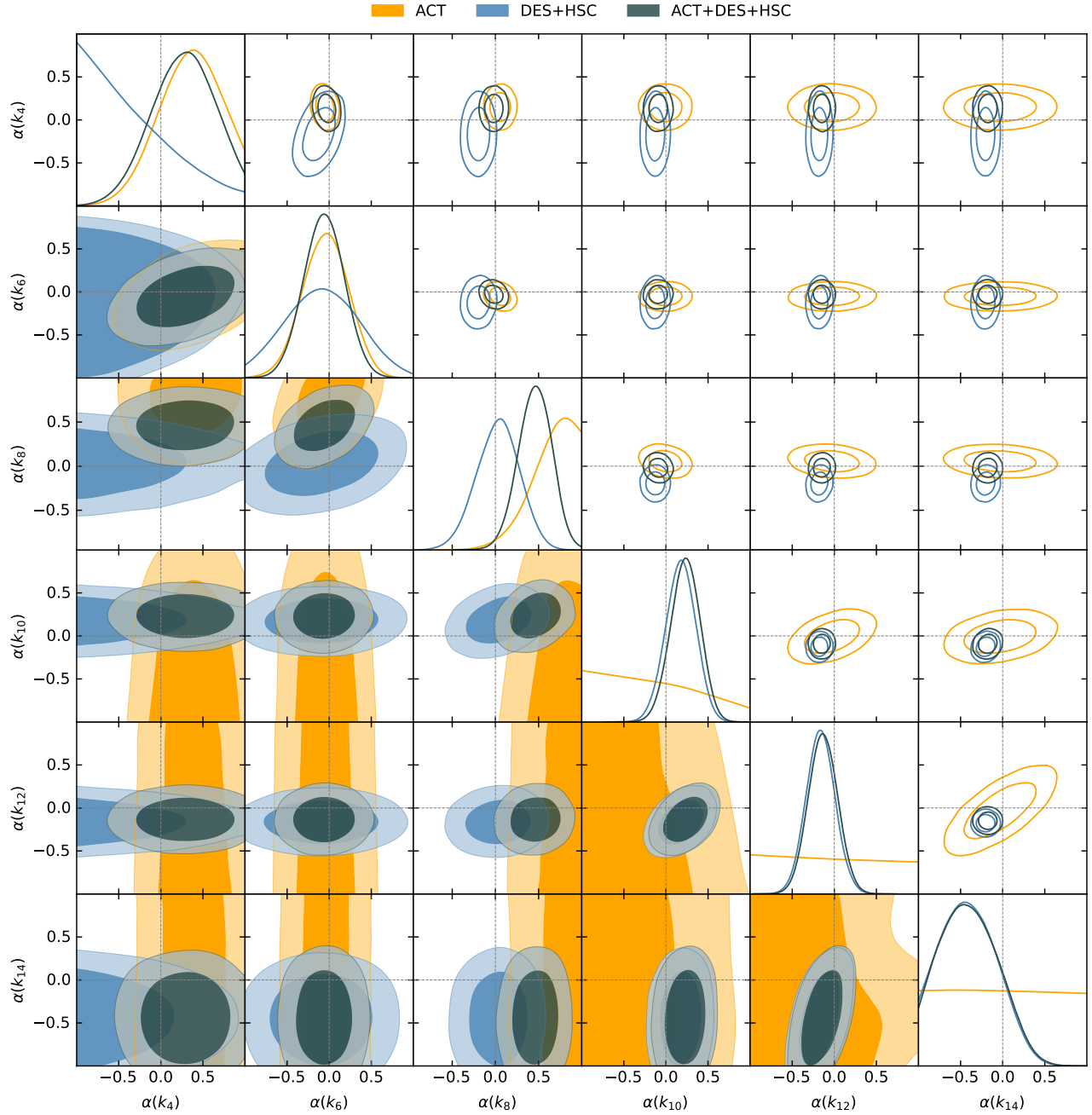


FIG. C1.— Constraints on  $\alpha(k)$  from ACT DR6 (yellow), DES Y3 combined with HSC Y3 (blue), and their combination (dark gray), using the uniform prior (lower triangle and diagonal) or the standard  $\sigma_s = 0.3$  smoothing prior (upper triangle). For readability, we only show every other  $k$ -bin in the range  $7 \times 10^{-3} \text{ Mpc}^{-1}$  to  $1.2 \text{ Mpc}^{-1}$  which is constrained by ACT+DES+HSC data. The effects of the prior are clearly visible in the lower triangle, while the upper one illustrates how the smoothed posteriors are Gaussian and mostly uncorrelated in the constrained range.

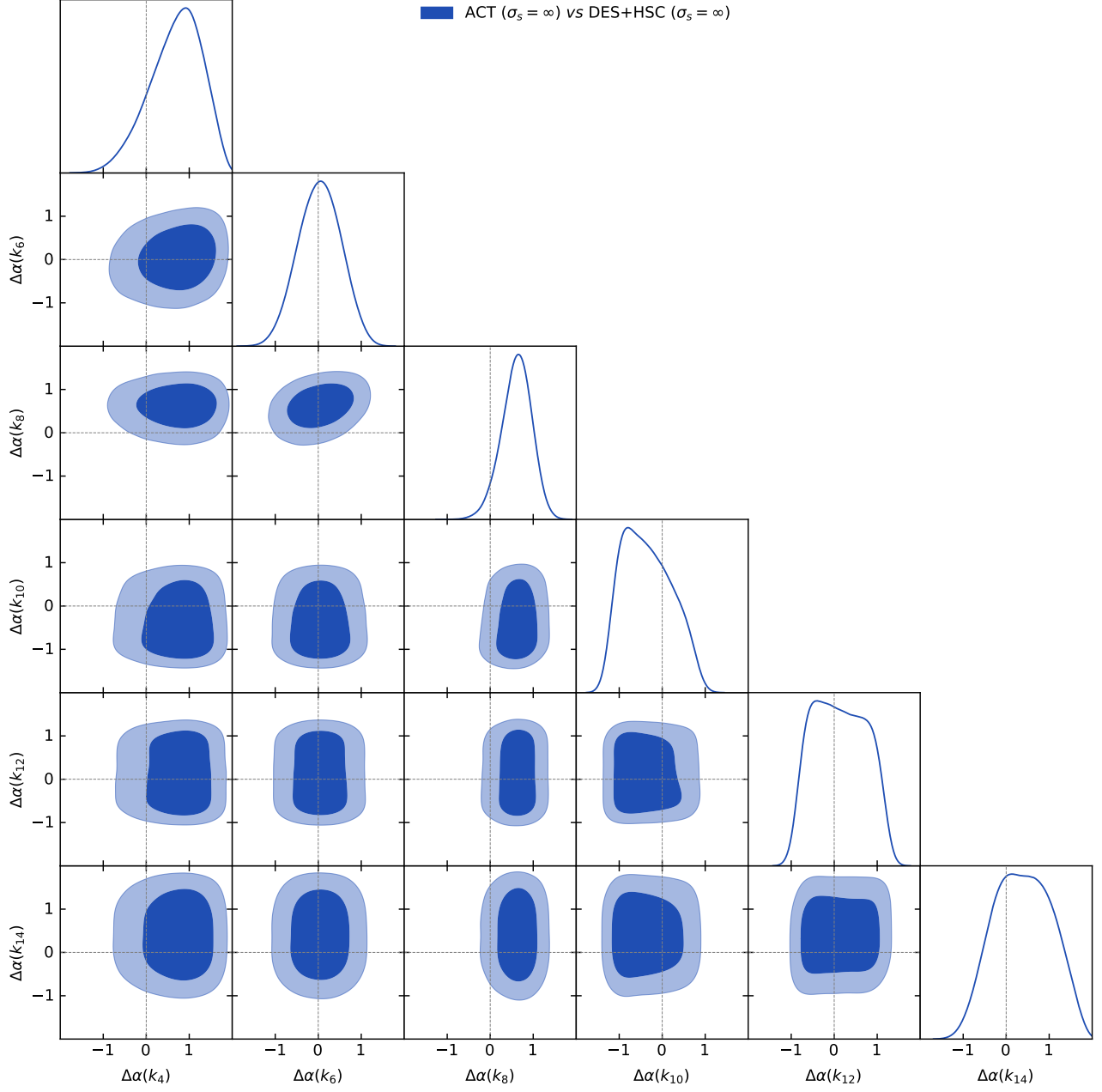


FIG. C2.— Marginals of the parameter-difference distribution between ACT and DES+HSC (uniform prior) for the same  $k$ -bins as Fig. C1. This figure illustrates the non-Gaussianity of the distributions due to prior boundaries. For this reason, we estimate consistency using the non-Gaussian metric in *Tensimeter*, corresponding to the volume of the difference distribution within the isodensity contour crossing the zero-difference point (see [Raveri and Doux 2021](#), for details).

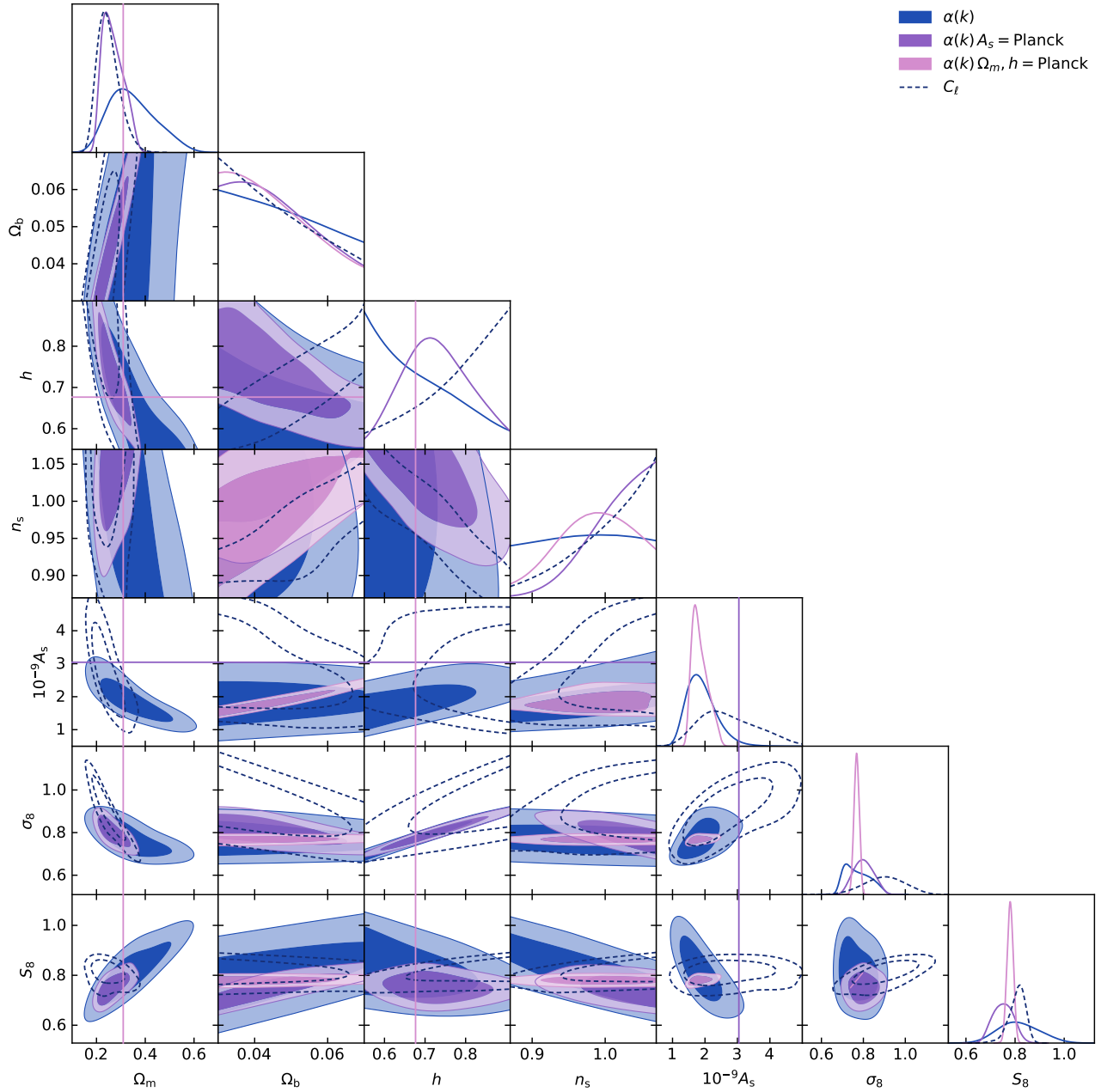


FIG. D1.— Comparison of constraints on  $\Lambda$ CDM parameters inferred from the derived  $\alpha(k)$  likelihoods and those obtained directly from the power spectra  $C_\ell$  for DES Y3 data. The blue contours vary all  $\Lambda$ CDM parameters, same as the  $C_\ell$  chains. We also draw a comparison with fixing  $A_s$  at the *Planck* fiducial value in Table 2 to isolate shifts in the overall amplitude of  $\alpha(k)$  in purple. Lastly, we also separately factor out the background cosmology by fixing  $\Omega_m$  and  $h$  to their fiducial values in pink. For both these cases, the values at which the  $\Lambda$ CDM parameters are fixed are marked by horizontal and vertical lines following the legend colors. None of these methods recover the same posterior footprint as the power-spectrum analysis.